Technische Universität Berlin
Institute of Software Engineering and Theoretical Computer Science
Neural Information Processing Group

Bachelor Thesis

Modelling functional connectivity in health and psychiatric disorders

Supervisor:
Prof. Dr. Klaus Obermayer
Prof. Dr. Manfred Opper

by:
Berk Can Özmen
396694

on 07.12.2020

Affidavit

I hereby declare that the thesis submitted is my own, unaided work, completed without any unpermitted external help. Only the sources and resources listed were used.

The independent and unaided completion of the thesis is affirmed by affidavit:

Berlin, 06.12.2020, _____

Signature

Abstract

The abnormalities that are caused by the anatomical disconnection in the structural spatio-temporal fluctuations among brain regions during rest (i.e resting-state functional connectivity) have well been related to schizophrenia, however, the underlying dynamics are still not well understood. In this work, we employ a grid search on the parameter space of a simple 2-dimensional excitable neuronal model, derived from the FitzHugh-Nagumo model and whose Hopf bifurcation is controllable by an external stimulus, in order to simulate a large scale brain network. We use three different data sets, that consists of subjects with schizophrenia and healthy controls, in order to show that regardless of the underlying structural connectivity, there exists a subset of parameters that give the best fit, however the goodness of fit might not only depend on the psychiatric condition of the subject, but also on the quality of the imaging.

Zusammenfassung

Die Anomalien, die durch die anatomische Trennung der strukturellen räumlich-zeitlichen Oszillationen zwischen Gehirnregionen während der Ruhezeit (d.h. resting state functional connectivity) verursacht werden, sind gut mit der Schizophrenie verbunden, aber die zugrunde liegende Dynamik ist jedoch noch nicht gut verstanden. In dieser Arbeit verwenden wir eine Rastersuche im Parameterraum eines einfachen zweidimensionalen Modells, das vom FitzHugh-Nagumo-Modell abgeleitet ist und dessen "Hopf bifurcation" durch einen externen Stimulus gesteuert werden kann, um ein "large scale brain network" zu simulieren. Wir verwenden drei verschiedene Datensätze, die aus Subjeckten mit Schizophrenie und gesunde Subjeckten bestehen, um zu zeigen, dass es unabhängig von der "structural connectivity" eine Teilmenge von Parametern existiert, die das bestes Ergebniss ergibt, die Qualität der Anpassung jedoch möglicherweise nicht nur davon abhängt, den psychiatrischen Zustand des Subjekts, aber auch die Qualität der Datensätze.

Acknowledgements

Table of Contents

1. Introduction

As Lynall [1] points out, ideas that relate psychiatric disorders and abnormal axonal connectivity, date back to 19th century psychiatrists such as Theodor Meynert and Carl Wernicke. During the recent years numerous evidence has been found linking the dysconnectivity between brain regions and schizophrenia, where this relationship can be observed at a physiological level [2, 3, 4]. Since then, analysis of abnormalities in resting state functional connectivity (rsFC), i.e correlation of fMRI data between brain regions acquired when the brain is not involved in an active task has been linked to the structural connectivity, that is the anatomical connection strength amongst the brain regions measured using diffusion tensor imaging [5, 6, 7, 8, 9, 10]. Despite the growing interest in rsFC research, a comprehensive model that can describe the underlying dynamics still cannot be found [5, 10].

The modeling approach is one of the most common approaches, where self sustaining chaotic oscillatory behavior as neural population activity is shown to be capable of describing some of the rsFC properties in macaque's cortex [11]. In the human cortex, we have not only identified the importance of local fluctuations and selection of the model [10, 12], but also the importance of introduced delay regarding the relationship of distance between brain regions and rsFC [13, 14],as well as the effects of local noise [15].

One of the biggest challenges of using a simulation approach is the rising computational cost as more parameters are introduced and as the used model gets more complex. Previously black box search optimization approaches such as genetic algorithms [16] have been used, however even though such methods are successful at finding optimal working points, they fail to present us an overall understanding of the parameter space. Therefore, in this study, we are employing a 4 dimensional grid search approach on a relatively simple model, i.e a derivation of the FitzHugh-Nagumo model, in order to be able to obtain a better understanding of the underlying dynamics. We have used 3 different data sets, one consisting of 11 schizophrenia patients, another data set from 15 healthy control subjects that are taken with the same imaging parameters as the schizophrenia patients and lastly 10 more healthy patient's data from a different study with different imaging parameters. Our purpose for this study is not only to be able to understand the effects of the psychiatric disorder and different imaging qualities on the predictions of the empirical rsFC, but also to be able to infer how is the underlying network effected by different parameter combinations depending on the used data set.

1.1. Terminology and Data Structure

This section includes abbreviations and information about data structure, see relevant section for more explanations.

Nodes and Number of Nodes (N): A node in the network means a region of interests labeled according to AAL [17] atlas. In our data, there are 94 identified regions, consisting of 80 cortical and 14 sub-cortical regions.

Structural Connectivity(SC) and Length Matrix(LM): Matrices $SC, LM \in \mathbf{R}^{N \times N}$ acquired by DTI, $SC_{i,j}$ indicates the connection strength between i^{th} and j^{th} nodes and $LM_{i,j}$ indicates the distance between i^{th} and j^{th} nodes.

Blood Oxygen Level Dependent Signal ($BOLD$): $BOLD \in \mathbf{R}^{N \times \cdot}$ data acquired by fMRI imaging, number of columns is dependent on the data-set.

Functional Connectivity (FC): $FC \in \mathbf{R}^{N \times N}$, $FC_{i,j} = correlation(BOLD_i, BOLD_j)$, where $correlation(\cdot, \cdot)$ returns Pearson Correlation Coefficient.

Functional Connectivity Dynamics (FCD): see 2.3.3

Conduction Velocity (c) and Delay Matrix (DM): c (scalar) defined in terms of mm/s, indicates how fast information transfers from one node to another. DM $DM \in \mathbf{R}^{N \times N}$ is calculated dividing length matrix by c. $c = \infty \implies DM$ is a matrix of ones

Global Coupling (K): (scalar) scaling factor for SC matrix.

External Stimulus (I_{ext}): (scalar), external stimulus for local FHN dynamics.

emp **or** *sim* **Prefix before matrices:** mean that matrix is acquired empirically or by simulation (for ex. $empFC$ or $simFC$).

Data-sets: 3 different data-sets: Greifswald (GW) (10 subjects) , healthy control (HC) (15 subjects) and schizophrenia patients (SCZ) (11 subjects) are used in this study. The notion of "intra-dataset" is used in order to state a comparison of any feature with two subjects that belong to the same data-set, and the notion of "inter-dataset"indicates a comparison between two subjects from two different data-sets (see Section 2.1)

1.2. Related Studies

In a 2020 study [18], that is the study we also have been inspired methodologically, a large scale parameter space exploration on the parameters global coupling K and conduction velocity c has been conducted using the Stefanescu-Jirsa Hindmarsh-Rose 3D model, that consists of 6 differential equations representing 3 excitatory and 3 inhibitory neural populations. The aim of the study was to show that there exists a unique subset of parameters for every individual (i.e SC) that can produce the best $simFC$-$empFC$ fit. We will briefly introduce the key findings related to how does the SC relates to the resting state functional connectivity, the role of parameter selection and the subject specificity, which also relates to our study.

Firstly, they have found out that the optimal coupling strength depends on the underlying SC in a linear fashion, such that for the increasing average SC weights, the optimal global coupling strength decreases. However the optimal coupling strength, being unique to the individual, occurs in a small range, where an intermediate amount of global coupling is needed for the coordination and synchronization in the system. A high level of global coupling strength causes biologically implausible levels of synchrony, and with low levels of K the large scale brain network creates disconnected nodes, with low correlations in between. This observation, that increasing K causes a globally connected BOLD signal, has also been shown for the FHN model in a different study by Vuksanovic [19].

However, while the selection of the coupling strength being very critical in order to recreate the rsFC, they have noted that, similar to the FitzHugh-Nagumo model, the Hindmarsh-Rose model is affected less by the conduction velocity, and optimal conduction speed can be found in a wider range of values.

The subject specificity of the model, i.e if the subject's own SC can predict the $empFC$ better than SC that belong to other subjects, has also been explored in this study, and they have concluded that due to lack of variability in SCs compared to the $empFC$s, the model was not able to produce subject specific predictions.Yet, they have shown that, not only the SC matrices, which could predict $empFC$ better, were also more successful at fitting the simulated FC to $empFC$, but also the $simFC$ matrices were more successful at predicting the $empFC$ compared to the SC alone.

Similarly, Messe [20, 21] argues that SC cannot account for the dynamics of resting state functional connectivity alone, but rather it is a cause behind the rsFC combined with the dynamics of the neural populations and its physiology. This can help us to understand why Triebkorn [18] was able to fit the $empFC$ with the simulated data better than the SC alone. However, as Cabral [12] argues, the goodness of fit between the simulated FC and the empirical FC depends not only on the properties of the mathematical model behind, but also on the quality of the SC.

Moreover, when Triebkorn [18] have compared the subject specificity on the $simFC$ and the SC correlations,the model was proved to be successful in reproducing subject specific $simFC$-SC correlations, and argued that this was an indicator of how strongly does the underlying SC shapes the $simFC$. Parallel to this observation, Messe[21] have examined the relationship between the underlying SC matrix and the simulated FC, using the FitzHugh-Nagumo model, and have noted that for even random, unstructured graphs the FHN model has resulted in high correlations of SC-$empFC$.

However, the role of conduction velocity largely depends on the selected model to represent the local dynamics. To the contrary of the stated insignificance of the conduction velocity for both the Hindmarsh-Rose and the FitzHugh-Nagumo model, Deco [11] has argued that for the Wilson-Cowan model, the introduced delay was playing an important role to create a plausible rsFC. Deco has explained the importance of the delay matrix (i.e conduction velocity) by stating that the SC was accounting for the spatial component of the FC, where the delay matrix captured the temporal component.

Also for Kuramoto model [12] and for a neural mass model [14], the conduction speed was identified as an important agent in order to explain the variances in the rsFC, that was unexplained by the SC alone, such that the introduced delay can prevent the "full synchronization of the network".

To create a biologically plausible rsFC, capturing the asynchrony is as much as important as describing the synchrony. Therefore, Deco [11] has discussed the role of noise that enables the anticorrelation patterns in the blood oxygen level dependent signal. Yet he notes that these complex dynamics could still be achieved in the absence of the noise and delay, to give a concrete example, Cabral [12] states that the local network oscillations in the Kuramoto model could account for a recreation of $empFC$ even without introducing noise.

Apart from the noise and the conduction velocity, the selection of local network dynamics affects how does the SC relate to the $empFC$.[15, 10, 22] have evaluated different oscillatory models such as Wilson-Cowan system, Hopf oscillators and the FitzHugh Nagumo model, where they both argued that the optimal operating regime for FC, FCD and meta-stability can be found near to the bifurcation points, i.e near to the edges of Hopf bifurcations that separates the limit cycle and the stable regions. The possible reason for this as explained by Deco is that: "at the edge of the critical instability of any model, the spatial correlations of the noisy excursions are mainly shaped by structure." [10].

2. Materials and Methods

2.1. Data Acquisition

Greifswald Data Set

The data consist of structural and resting state fMRI acquired from 10 older adults (6 females; females: age range = 52-77 years, mean age = 65.5 years, standard deviation of age = 10.178 years; males: age range= 55-78 years, mean age= 67.25 years, standard deviation of age = 8.437), and is a subset of a data acquired in a study from Universitätsmedizin Greifswald with 27 participants. The study was approved by the local ethics committee at Universitätsmedizin Greifswald and was in accordance with the Declaration of Helsinki. All participants gave their written informed consent prior to taking part in the study and were reimbursed for their participation.

Structural imaging data: Data acquisition was performed using a 3T Siemens MAGNE-TOM Verio syngo B17 MR scanner with a 32-channel head coil. High-resolution anatomical T1 images were acquired using a gradient echo sequence (TR = 1690 ms, TE = 2.52 ms, TI = 900 ms, flip angle (FA) = 9 °, FOV = 250 x 250, matrix size = 246 x 256, slice thickness = 1 mm, number of slices = 176), while for diffusion data a single-shot echo-planar imaging (EPI) sequence (TR = 11100 ms, TE = 107 ms) was used. For every subject, there were 64 gradient directions (b = 1000 s/mm 2) and one non-diffusion-weighted acquisition (b = 0 s/mm 2) acquired over a field of view of 230 x 230 x 140 mm, with a slice thickness of 2 mm and no gap, and a voxel size of 1.8 x 1.8 x 2 mm.

Preprocessing of T1- and diffusion-weighted images was conducted using a semi-automatic pipeline implemented in the FSL toolbox (`www.fmrib.ox.ac.uk/fsl`, FMRIB, Oxford). Preprocessing of anatomical T1-weighted images involved the removal of non-brain tissue using the brain extraction toolbox (BET) implemented in FSL, as well as the generation of a brain mask. The quality of the brain-extracted images was assessed manually and subsequently, 94 cortical and subcortical regions were defined based on the automatic anatomical labeling (AAL2) atlas introduced in [17]. Brain extraction was also conducted for the diffusion-weighted images, and it was followed by head motion and eddy current distortion correction. Subsequently, a probabilistic diffusion model was fitted to the data using the Bayesian Estimation of Diffusion Parameters Obtained using Sampling Techniques (BED-POSTX) FSL toolbox. Individual connectomes were obtained by linearly registering each subject's b0 image to the corresponding T1-weighted image, transforming the high-resolution mask volumes from MNI to the individual's diffusion space and running probabilistic tractography with 5000 random seeds per voxel using FSL's PROBTRACKX algorithm [23]. Furthermore, as probabilistic tractography contains no directionality information, but is dependent on the seeding location, the connection strength $SC_{i,j}$ between regions i and j was considered equal to the connection strength $SC_{j,i}$ between regions j and i and was obtained by averaging the corresponding entries in the connectivity matrix. Each connectivity matrix was normalized by dividing every matrix entry by the maximum value of the matrix.

Resting-state functional MRI data: Resting-state functional MRI data were acquired using the same 3T Siemens MAGNETOM Verio syngo B17 MR scanner, with the following parameters: TR = 2000 ms, TE = 30, slice thickness = 3 mm, spacing between slices = 3.99 mm, FA = 90 ° , matrix size = 64 x 64, FOV = 192 x 192, voxel size = 3 x 3 x 3 mm. Participants were scanned for 12 minutes, leading to an acquisition of 360 volumes per participant.

Preprocessing of rsfMRI data was conducted using the FSL FEAT toolbox [24]. The first five volumes of each data set were discarded. Data were corrected for head motion using the FSL McFLIRT algorithm, and high-passed filtered with a filter cutoff of 100s. Functional images were linearly registered to each subject's anatomical image using FLIRT. A brain mask was created from the mean volume of the data using BET. MELODIC ICA was conducted and artefactual components (including motion, non-neuronal physiological artefacts, scanner artefacts and other nuisance sources) were removed using the ICA FIX FSL toolbox [25, 26]. Subsequently, the high-resolution mask volumes were transformed from MNI to individual subject functional space and average BOLD time courses for each cortical region were extracted using the fslmeants command included in Fslutils.

HC & SCZ Data Set

The data consist of structural and resting state fMRI acquired from 15 healthy adults (HC) and 11 adults with schizophrenia (SCZ). (SCZ data: 3 females; females: age range = 22-56 years, mean age = 43.0 years, standard deviation of age = 14.989 years; males: age range= 19-55 years, mean age= 32.875 years, standard deviation of age = 13.11. HC data: 6 females; females: age range = 18-54 years, mean age = 30.667 years, standard deviation of age = 11.746 years; males: age range= 24-52 years, mean age= 34.111 years, standard deviation of age = 11.12.) and obtained from the SchizConnect database (`http://schizconnect.org`). The study was approved by the local ethics committee and all participants gave their written informed consent prior to taking part in the study.

Structural imaging data: Data acquisition was performed using a Siemens Magnetom Trio 3T MR scanner. High-resolution T1 weighted images were acquired using a five-echo MPRAGE sequence (TR = 2530ms, TE = 1.64, 3.5, 5.36, 7.22, 9.08 ms, TI = 1200 ms, flip angle (FA) = 7 ° , FOV = 256 x 256 mm, matrix size = 256 x 256, slice thickness = 1 mm, number of slices = 192), while for diffusion data a single-shot echo-planar imaging (EPI) sequence (TR = 9000 ms, TE = 84 ms) was used.

For every subject, there were 30 non-collinear diffusion gradient directions (b = 1000 s/mm2) and 5 non-diffusion-weighted acquisition (b = 0 s/mm2) equally interspersed between 30 gradient directions acquired over a field of view of 256 x 256 mm, matrix = 128 x 128 with a slice thickness of 2 mm and no gap, 72 axial slices, flip angle (FA) = 90 °.

Preprocessing of anatomical and diffusion images was conducted using a semi-automatic pipeline implemented in the FSL toolbox (`www.fmrib.ox.ac.uk/fsl`, FMRIB, Oxford). Preprocessing of anatomical T1-weighted images involved the removal of non-brain tissue

using the brain extraction toolbox (BET) implemented in FSL, as well as the generation of a brain mask. The quality of the brain-extracted images was assessed manually and subsequently, 94 cortical and subcortical regions were defined based on the automatic anatomical labeling (AAL2) atlas described in [17].

For diffusion data, we performed brain extraction on the b0 images using BET. After correcting the data for head movement and eddy current distortions, we fitted a probabilistic diffusion model to the data by using the Bayesian Estimation of Diffusion Parameters Obtained using Sampling Techniques (BED-POSTX) FSL toolbox. Finally, we linearly registered each b0 image to the corresponding subject's anatomical T1 image, transformed the high-resolution anatomical mask volumes containing the cortical parcellations to the subject's diffusion space, and ran probabilistic tractography with 5000 samples per voxel using FSL's PROBTRACKX algorithm [23].

2.2. Simulation and Parameters
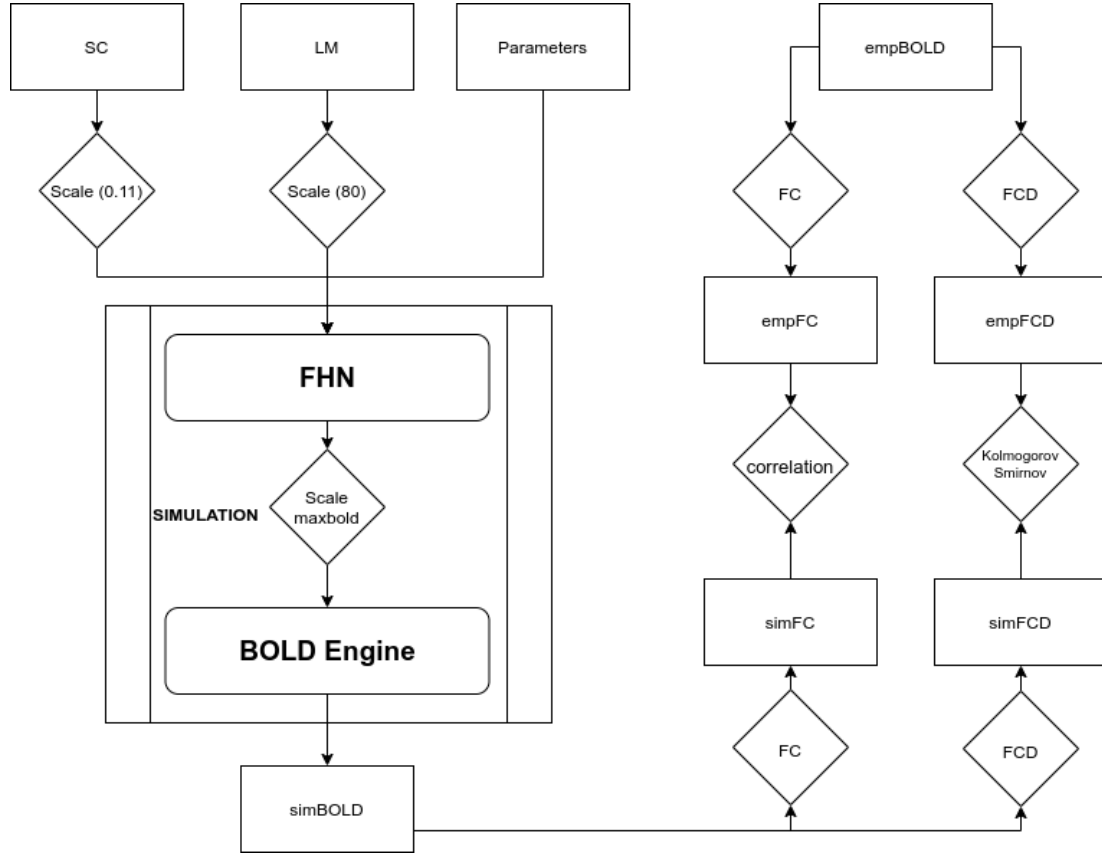
Fig. 2.1: Simulation Diagram and Evaluation Scheme of the Output $simBOLD$

A single simulation takes 3 inputs, a scaled SC matrix, a scaled LM matrix, and a set of parameters (I_{ext},K,c,σ,$maxbold$), and consist of two steps, the FHN network and the BOLD Engine (input:scaled FHN output), and outputs the $simBOLD$. The evaluation scheme of the $simBOLD$ for a given $empBOLD$ consists of two parallel processes. Firstly, we convert the $simBOLD$ into the $simFC$ and the $empBOLD$ into $empFC$, then we take the Pearson correlation coefficient of two matrices. Secondly, we convert the $simBOLD$ into the $simFCD$ and the $empBOLD$ into the $empFCD$, and then calculate their Kolmogorov-Smirnov Test D-statistic as a measure of distance.

In order to acquire a good understanding of the effects that imaging quality, psychiatric disorder (schizophrenia) and different parameter combinations have on the functional connectivity modeling, we have conducted a grid search through 4 different parameters using data acquired by 36 subjects. The simulation architecture is summarized in the Fig.2.1 and the same architecture is used for all 36 subjects and all the parameter combinations. We have modeled every 94 regions using FitzHugh-Nagumo Model (FHN), in order to acquire a simulated neural activity using the scaled structural connectivity (SC) matrix, scaled length matrix (LM) and 4 different parameters to describe the communication between different regions and the dynamics of the FHN model. Then, the simulated neural activity is linearly scaled to a range of $[0, max\_bold]$ and converted into the blood level dependent fMRI signals ($simBOLD$) using the hemodynamic model (BOLD Engine) [27], later the $simBOLD$ is down-sampled by deleting all the entries except every 20000th (20000 entry = 2 sec-

onds), in order to match with the empirical $BOLD$ that is acquired every 2 seconds. The simulated functional connectivity ($simFC$) and simulated functional connectivity dynamics ($simFCD$) matrices are then calculated using the down-sampled $simBOLD$ signals, which are later compared with the empirical data. All the down-sampled $simBOLD$ signals are saved for later use, all the code used and the result matrices are accessible under `https://github.com/bcozmen/grid_data`.

2.2.1. Scaling of SC and LM Matrices

Since we are using 3 different data-sets, that were acquired in two different studies with different imaging parameters, it is important to note that, both SC and LM matrices have different average degrees (mean of row sums) depending on the data set. The parameter K is dependent on the underlying SC and other studies using different models have found a linear relationship between average degree and the parameter K [18, 28]. Thus, in order to be able to get a meaningful and comparable result, we have decided to scale SC and LM matrices, so that they will have the same mean (scaled to the mean of GW data-set, 0.11 for SC and 80 for LM). Since both of K and c parameters are used as linear operations, this should have no fundamental effect on our FHN network.

2.2.2. FitzHugh-Nagumo Model (FHN)

The FitzHugh-Nagumo Model (FHN) first introduced by Richard FitzHugh [29], is a 2 dimensional non-linear relaxation oscillator. It is a model of an excitable neuron with 2 state variables, closely related to the Hodgkin-Huxley model. The 2 state variables u and w can be described by the following differential equations

$$\dot{u} = \tau(u - \frac{u^3}{3} + w + I_{ext}) \tag{2.2}$$

$$\dot{w} = -\frac{1}{\tau}(u - \alpha + \beta w) \tag{2.3}$$

where, u describes the membrane potential, w can be identified as the refractory parameter and I_{ext} is the external stimulus.

Local Dynamics

In this study, we are going to be using a derivation of the FHN model for modeling the behavior of a single node. The equations for local dynamics are given by:

$$\dot{u} = h(u, w, I_{ext}) = -\alpha u^3 + \beta u^2 + \gamma u - w + I_{ext} \tag{2.4}$$

$$\dot{w} = g(u, w) = \frac{1}{\tau}(u + \delta - \epsilon w) \tag{2.5}$$

where $\alpha = 3, \beta = 4, \gamma = -1.5, \delta = 0, \epsilon = 0.5$, and $\tau = 20$ where τ controls the frequency of oscillation . The parameters are taken from Kostova [30] in order to obtain similar bifurcation behavior, and slightly modified to make it more similar to the phase diagram of the ALN model [31]. The idea behind this derivation, is to be able to create a bifurcation diagram (see Fig.2.6b) depending on the parameter I_{ext}, where for $I_{ext} < 0.7$ the parameter u is in its low state, and for $I_{ext} > 1.35$, the parameter u is in its high state, and in the limit cycle for the rest of the values (see Fig. 2.6a).

(a) Activity of derived FHN model

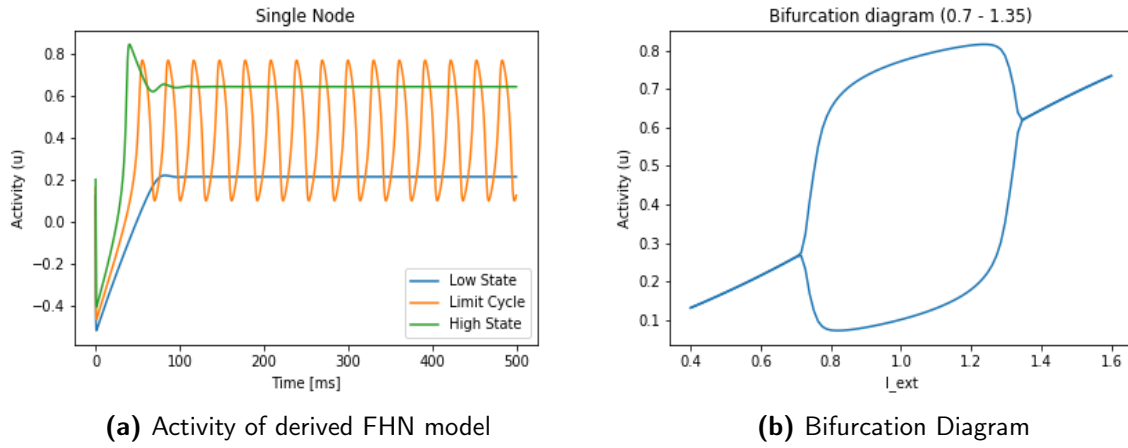**(b)** Bifurcation Diagram

Fig. 2.6

Global Dynamics

Global dynamics refers to how does the different nodes interacts with each-other. Every single node is characterised by the equations 2.4. Here, we introduce 3 more parameters, K, c and σ in order to define the relationship between these nodes. K is the global coupling strength, that is used to scale the SC matrix, where $K \cdot SC_{i,j}$ specifies the connection strength between node i and j. c refers to the conduction velocity, that is used implicitly in the delay matrix (DM) such that $DM = \frac{LM}{c}$. $DM_{i,j} = LM_{i,j}/c$ gives the delay between node i and j. Thus, the information transfer between node i and j is affected by both DM and SC, such that the first derivative of the activity at the ith node at time t is increased by $K \cdot SC_{i,j}$ times activity at the jth node at time $t - DM_{i,j}$. Lastly σ denotes the standard deviation of the Gaussian noise added to the change rate of activity. The global dynamics of the network for i^{th} node u_i is characterized by the following equation:

$$\dot{u}_i(t) = h(u_i(t), w_i(t), I_{ext}) + K(\sum_{j=0}^{j=N} SC_{i,j}u_j(t - DM_{i,j})) + \sigma\eta(t) \tag{2.7}$$

where, $\eta(t) \sim \mathcal{N}(0, 1)$, and $\dot{w} = g(u, w))$ (see Eq. 2.5). For given scaled SC, LM and

parameters, we have simulated Eq.2.7 and Eq.2.5 using 4th order Runge-Kutta method with the step-size=0.1, by setting $u_i(0) = 0$ and $w_i(0) = 0 \ \forall i$.

2.2.3. The Hemodynamic Model

The hemodynamic model (HDM) [27, 32], is a non linear dynamic model that describes the relationship between neuronal activity and the blood oxygen level dependent fMRI signal. The HDM combines two models, a linear dynamic model that relates the neuronal activity to regional cerebral blood flow (rCBF) and the Balloon/Windkessel model, that links rCBF to the $BOLD$ signal. For neuronal activity z the first part of the model is given by the following equations:

$$\dot{s} = z - \kappa s - \gamma(f_{in} - 1) \tag{2.8}$$

$$\dot{f_{in}} = s \tag{2.9}$$

where f_{in} describes the rCBF and the rate of increase is proportional to the neural activity in order to compensate for metabolic oxygen need. s is an activity dependent flow inducing signal, $\kappa = 0.65$ defines the rate of signal decay and $\gamma = 0.41$ is the rate of flow-dependent elimination that acts as an auto-regulatory feedback.

The Balloon component is described by:

$$\tau\dot{v} = f_{in} - f_{out}(v) \tag{2.10}$$

$$\tau\dot{q} = \frac{f_{in}E(f_{in}, \rho)}{\rho} - \frac{f_{out}(v)q}{v} \tag{2.11}$$

$$f_{out}(v) = v^{\frac{1}{\alpha}}$$

$$E(f, \rho) = 1 - (1 - \rho)^{\frac{1}{f}}$$

where, v describes the venous volume, whose rate of change is simply described by the difference between amount of inflow and outflow and effected by the hemodynamic transit rate $\tau = 0.98$, that express the average time to travel through or refill the venous compartment.

The total volume of blood is a factor, since the fMRI technique that measures the blood oxygenation level, exploits the magnetic properties of the deoxyhemoglobin (q as described in the Eq:2.11), thus is affected by both deoxyhemoglobin amount and the total blood volume.

Furthermore, the oxygen that is extracted by the tissue in order to meet the metabolic demand, that causes a change in blood oxygenation level, is modeled in the Eq:2.11 by the function $E(f_{in}, \rho)$, where $\rho = 0.34$ is the resting oxygen extraction fraction. Here, in the first part of the Eq:2.11, the rate of oxygen use (hence the change in deoxyhemoglobin) is affected by the incoming blood flow and the rate which oxygen is extracted from the blood into the tissue.

And lastly, the simulated $BOLD$ signal is given by a weighted sum of deoxyhemoglobin and the blood volume:

$$simBOLD = V_0(k_1(1-q) + k_2(1 - \frac{q}{v}) + k_3(1-v)) \tag{2.12}$$

where $k_1 = 7\rho \mid k_2 = 2 \mid k_3 = 2\rho - 0.2 \mid V_0 = 0.02$.

For given z (that is the FHN output of all of the 94 nodes), we have first calculated maximum (max_z) and minimum values (min_z) in z, then we have scaled every z_i (that is the FHN output of ith node) from the range $[min\_z, max\_z]$ to $[0, maxbold]$, so that we wouldn't be losing the relative amplitude information. Then we have calculated $BOLD_i$ from z_i simulating the hemodynamic model using the forward Euler method and with the step-size=10^{-4}, where we have set $s_i(0) = f_i(0) = v_i(0) = q_i(0) = 1$. Lastly, we have down-sampled the $BOLD$ signal by deleting every entry except the 20000th (one sample for every 2 seconds as in the empirical data) and we have also discarded the first 50 entries of down-sampled $BOLD$ signal, since the initialization phase until the equations reaches an equilibrium were very similar for every node that boosted the correlation values.
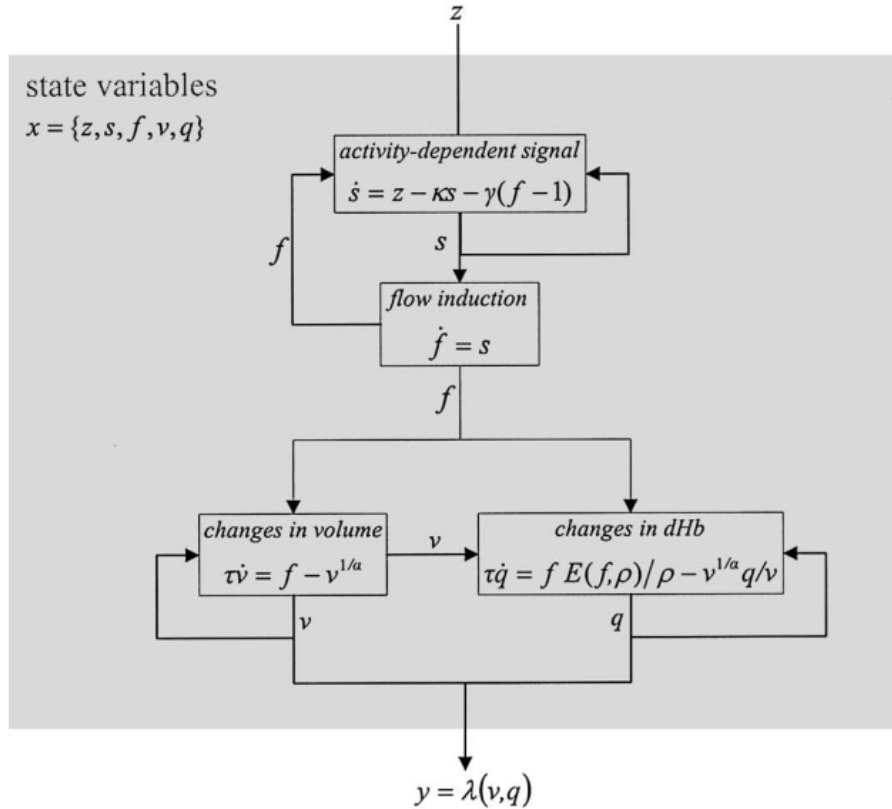
Fig. 2.13: The hemodynamic model. Source:[27]

A visualization of the hemodynamic model for a single region. The neuronal activity (z) induces the activity dependent signal (s) which increases blood flow (f). As a consequence, flow causes an increase in volume (v) and deoxyhemoglobin (q). The relevant BOLD signal (y) is calculated as a weighted sum of v and q as in Eq.2.12

2.2.4. Parameter Space and Simulation Details

Parameter Space

Table 1: Parameter space

Parameter	Values	Number of points
I	[0.2 : 1.2 : 0.025]	41
K	[0.2 : 1.2 : 0.025]	41
c	[0 : 100 : 20] + [5,10]	8
σ	[0.05, 0.01, 0.005, 0.001, 0.0005, 0.0001,0]	7
$maxbold$	60	1

The simulations were performed on the HPC cluster of the TU Berlin for 36 subject data in Python3 and the numba library was used for efficient computing. The FHN equations were implemented using the 4th order Runge-Kutta method, and the hemodynamic model was calculated by the forward Euler method for the parameters described in Table 1 (94136 different parameter combination per subject), with time step = 0.1 (FHN) and 0.0001 (BOLD), and for at least 390000ms in real time (for GW data-set 810000ms), matching with real duration of $empBOLD$ samples and $simBOLD$ outputs are down-sampled by 2000ms. Even though the duration of simulation has an effect on the magnitude of the noise in $simFC$-$empFC$ correlation (also depending on the σ value), we have observed that this effect shrinks with increasing duration.

The parameter ranges described in Table 1 are chosen with the previous knowledge based on explorations of the GW data-set using genetic algorithms. Both for highest and lowest values of I and K, we have observed that the FHN network already dies due to either low levels or high levels of activity, and cannot sustain an oscillatory behavior. (see 3.2), c values are chosen as bio-physically plausible [18] and σ values are chosen such that, we could explore both effects of high, mid, and low noise levels.

For $maxbold$ parameter, we had a prior belief (again from explorations using genetic algorithms) that the effect of this parameter was negligible, and in order to decrease the number of simulations, we have set the parameter to a constant. The effects of the parameter $maxbold$ will be discussed in chapter 3.

2.3. Metrics and Data Analysis

2.3.1. Pearson Correlation Coefficient

Pearson correlation coefficient is widely used in related researches in order to measure similarity between matrices [18, 22]. In this study, we have used correlation to evaluate similarity

between FC-FC, SC-SC and SC-FC matrices. Since all of the mentioned matrices are symmetric and one on diagonal, we have considered only the upper triangle excluding the diagonal of these matrices.

2.3.2. Functional Connectivity (FC)

FC matrix captures the statistical dependence of different brain regions. For node i and j, $FC_{i,j} = correlation(BOLD_i, BOLD_j)$, where $correlation(\cdot, \cdot)$ denotes the Pearson correlation coefficient and is evaluated using `numpy.corrcoef` function.

2.3.3. Functional Connectivity Dynamics (FCD)

FCD is a metric that aims to capture the change in FC [18, 33] over time and it is used in schizophrenia research [34] (as cited in [18]). In this research, we have calculated FC matrices with a sliding window over the down-sampled $BOLD$ signal with a window size = 30 time-step (60 seconds) and step size = 5 (10 seconds), and created a FCD matrix, such that $FCD_{t_i,t_j} = correlation(FC_{t_i}, FC_{t_j})$, where FC_{t_i} is the FC matrix calculated in the ith window. Therefore, the shape of the FCD matrix depends on the length of the simulation (see 2.2.4).

2.3.4. Kolmogorov-Smirnov (KS) Test

KS test is a non-parametric test with a null hypothesis that two samples are drawn from identical distributions. The D-statistics of KS-Test is calculated as the maximum distance in the y-axis (i.e. maximum distance keeping the x value constant) of the cumulative distributions functions given 2 probability distribution and the p-value is calculated from D-statistics. KS-Distance (D-statistics) is used as a measure of the distance between two FCD matrices [18, 22] and computed using `scipy.stats.ks_2samp` function. In this study, we are also going to use the KS-Test, in order to test the hypothesis that if two samples are drawn from identical distributions.

2.3.5. Simulation Results and Plots

In order to investigate subject specificity, differences in subjects with schizophrenia and healthy controls, possible effects of different imaging qualities, and possibly other factors, we have simulated 36 different SC and LM matrices at 94136 parameter combinations (41 values of I_{ext} and K in the range $[0.2, 1.2]$, 8 values of c in the range $[0, 100]$ and 7 values of σ in the range $[0, 0.05]$ in log space), resulting in 3388896 $simBOLD$ matrices. In order to interpret the data, we have further processed data into 6 different matrices and related information for the matrices are encoded as a Python dictionary (see 2.2).

The general matrix encoding is in shape $\in \mathbf{R}^{(36\times36\times41\times41\times8\times7)}$, where it corresponds to (first data$\times$second data$\times I_{ext} \times K \times c \times \sigma$).

- Correlation of $simFC$-$empFC$ under "corr_emp.mat", where first axis is the $simFC$ belonging to $index_1$ and second axis is the $empFC$ belonging to $index_2$

- Correlation of $simFC$-$simFC$ under "corr_sim.mat", where first axis is the $simFC$ belonging to $index_1$ and second axis is the $simFC$ belonging to $index_2$

- KS distance of $simFCD$-$empFCD$ under "ks_emp.mat", where first axis is the $simFCD$ belonging to $index_1$ and second axis is the $empFCD$ belonging to $index_2$

- KS distance of $simFCD$-$simFCD$ under "ks_sim.mat", where first axis is the $simFCD$ belonging to $index_1$ and second axis is the $simFCD$ belonging to $index_2$

- Correlation of $simFC$-SC under "simFC_SC.mat", where first axis is the $simFC$ belonging to $index_1$ and second axis is the SC belonging to $index_2$

- Kuramoto order parameter of $simBOLD$ under "kuramoto_bold.mat" $\in \mathbf{R}^{(36\times41\times41\times8\times7\times2)}$, where first axis is the $simBOLD$ belonging to $index_1$ and the last axis $=0$ for mean of Kuramoto order parameter, and $=1$ for standard deviation of Kuramoto order parameter
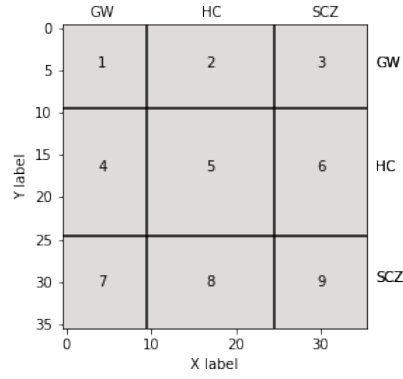
Cross Subject Matrices

In order to further simplify the data mentioned above, we have created cross subject matrices (as in [18]), where Matrix $M \in \mathbf{R}^{(36\times36)}$, such that $M_{i,j}$ is the maximum/minimum (depending on the context) of the related matrix belonging to $index_i$ and $index_j$. For example, cross subject matrix for $simFC$-$empFC$ matrix has at $M_{i,j}$ the best possible correlation value that we could get using $simFC$ belonging to individual i, and $empFC$ belonging to individual j. In order to plot the matrices, the convention below is used:

Parameter Space Plots

To be able to visualize the results, we have plotted $8 \times 7 = 56$ different image with resolution (41$\times$41), where images are identified by their c and σ values on rows and columns, and the y (vertical) axis of every individual image is used for I_{ext} value and the x (horizontal) axis is used for K values. The related information are provided as image title, and the used color map can be found under the image.

2.3.6. Kuramoto Order Parameter

In order to evaluate the synchrony amongst brain regions and the evolution of the synchrony over time (or metastability), we have used Kuramoto order parameter [35] $R(t)$, which is defined as,

Fig. 2.14: Example for Cross Subject Matrix

Data-set names indicates which data-set does the column/row belongs, and numbering are to refer specific combination of data-set

$$R(t) = \left| \frac{1}{N} \sum_{n=1}^{N} e^{i\varphi_n(t)} \right|, \quad R(t) \in [0, 1]$$

where $\varphi_n(t)$ is the instantaneous phase of nth region at time t, computed as,

$$\varphi(t) : \mathbb{N}_0 \mapsto [0, 2\pi], \quad \varphi(t) = 2\pi \frac{t - t_i}{t_i - t_{i-1}}$$

,where t_i is the time index of ith local maximum of the input time series, such that t_i and t_{i-1} denotes the next and previous local maximum with respect to the t and $t_{i-1} < t < t_i$. The given time series is smoothed using `scipy.ndimage.filters.gaussian_filter` function, and after that the indices of local maximums are detected using `scipy.signal.find_peaks`. The instantaneous phase $\varphi(t)$ is then calculated for every t using the formula above and the indices of local maximums, and lastly we have calculated the Kuramoto order parameter $R(t)$ for every time step t using $\varphi_n(t)$. The mean of $R(t)$ is used as a measure of syncrony, and the standard deviation of $R(t)$ is used as a measure of metastability.

The idea behind the Kuramoto order parameter as a measure of synchrony, is that first we detect instantaneous phase of every node n for time t, and then place their phases at time t on a unit circle to calculate their center of mass. The distance between center of mass and the origin of the unit circle gives us the $R(t)$ value for time t. The closer all of the phases are to each other, the closer is the center of mass to the unit circle, hence the $R(t)$ value gets closer to 1, where if all the phases are equal at time t (full synchrony), we get the center of mass on the unit circle. Therefore, when we average the $R(t)$ over time, we get the overall synchrony.

Similarly if two oscillators have different phases, thus different angular velocity on the unit circle, the position of center of mass changes over time, hence cause the $R(t)$ increase or

decrease over time, for that reason we can see the evolution of synchrony over time in the standard deviation of $R(t)$.

2.3.7. Similarity of Optimal Working Points

One of the question we aim to answer is how is the optimum parameter combination affected by the SC and/or $empFC$ matrix. However, this is not a trivial task due to numerous reasons.

Incommensurability of Parameters

First of all, since we have searched a 4-dimensional parameter-space, the natural thing to expect is to have a distance measure that takes into account all of the 4 parameters. The first problem we have encountered is that, we believe that the variation in parameters are not the same or even similar, s.t for the FHN model we expect that changing the value of c would have significantly less effect than changing other parameters as e.g. Triebkorn [18] have discussed: "The Hindmarsh-Rose local neural model is similar to the FitzHugh-Nagumo, where time delays were not critical in shaping network dynamics.", and this was also our observation from our previous exploration of the parameter space using genetic algorithms. Thus, we believe that, compressing a 4 dimensional information to only a single parameter would not be a good way of representing the data.

Secondly, our parameter space grids are not quantized either using the same resolution or with the same scale (i.e σ in log scale), therefore, in order to cope with the problems above, we have decided to evaluate the I_{ext}/K and c/σ spaces separately.

Discrete Search Space with Multiple Best Fit Points

When we investigate the I_{ext}/K parameter-space, we saw that, there isn't a best optimal parameter combination, rather there are regions that have similarly high correlation values. Also due to randomness included in the FHN network, we have observed that, especially with high σ values, the output correlation values have some degree of noise, which could potentially cause us to detect false optimal points. In order to cope with this problem, we have decided to not only consider best single parameter combination, but rather a set of optimal parameters.

This approach however poses two new problems, namely how many points should we consider in the optimal points set, and how can we quantify similarity of two sets of parameter. For the first problem, we have two constraints, if we choose our set too large, there will be many low correlation points that are identified as (false) good fits included in the set, if we choose the set too small, we might not account for the noise and we may not represent the optimal regions well enough.

In order to solve the first problem, we calculate the relative and absolute difference between the nth best $simFC$-$empFC$ correlation value and the best fit correlation for every individual-

to-individual fit (see Fig.2.19), and plot the mean of the values by data-set. Here we observe that the relative and absolute difference increases very quickly for the first 8 to 10 points regardless of the data set, therefore we heuristically decide for a set size = 15, where the mean absolute difference is 0.0213, about what we expect as the noise included in the FHN output (see section 4). When we scatter plot the best 15 points of every individual-to-individual fit parameters I_{ext}/K parameter-space (see Fig.2.20), we see that for the majority of individuals, we were able to represent a clustered set of points.

The second problem is not trivial to solve. For sets X and Y, we define distance as $D(X,Y) \in \mathbf{R}^+ \cup \{0\}$, such that:

$$D(X,Y) = \sum_{x \in X} \sum_{y \in Y} f(x,X,y,Y) \cdot d(x,y)$$

where, $d(x,y)$ is an arbitrary distance function, and $f(x,X,y,Y)$ a weight function, given point $x \in X$ and $y \in Y$, outputs a value in range $[0,1]$. Consider the following example:
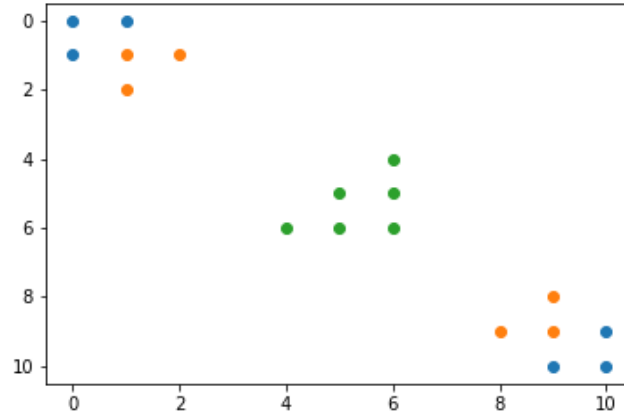

Fig. 2.15: An example similarity problem

where we want to decide if the green set or the orange set is more similar to the blue set. For our purpose, the solution is trivial, however depending on how do we choose $f(\cdot)$ and $d(\cdot)$, we could get either answer. The problem exemplified above can be solved by a $f(\cdot)$ function, that favors densely clustered points and penalizing distant clusters, however it is not trivial to find such a function.

Gaussian Kernel Density Estimation

In order to solve the problem mentioned at Fig. 2.15, and to bypass finding a function $f(\cdot)$ explicitly, we have decided to compute a probability distribution function (pdf) using (multivariate) Gaussian kernel density estimation (Gaussian KDE).

Kernel density estimation (ref:[36, 37, 38]) is a non-parametric way of estimating probability density function from given data points. The idea stems from the averaging of shifted histograms, but instead a non-negative, symmetric and multivariate density is applied as kernel function K to the individual data points, and the resulting density f is computed by a weighted sum of individual densities. The simplified form of a kernel density estimator is as follows [38]:

$$\hat{f}(x) = \frac{1}{nh^d} \sum_{i=1}^{n} K\{(x - X_i)/h\} \tag{2.16}$$

and $K : \mathbf{R}^d \mapsto \mathbf{R}$ is a d-variate kernel function satisfying:

$$\int K(x)dx = 1 \tag{2.17}$$

where d is the dimension, h is the bandwidth and n is the number of data points. Mostly the selection of the kernel function K is not very important [38], thus we have used multivariate normal density function:

$$K(x) = (2\pi)^{-\frac{d}{2}} e^{(-\frac{1}{2}x^T x)} \tag{2.18}$$

and Scott's rule is applied as the bandwidth [36]:

$$h = n_{eff}^{-\frac{1}{d+4}}$$

where

$$n_{eff} = \frac{(\sum_{i=1}^{n} w_i)^2}{\sum_{i=1}^{n} w_i^2}$$

is used where w is the weight vector, that consist of correlation values of points passed to KDE function. For the numerical calculations of KDE, `scipy.stats.gaussian_kde` implementation is used.

An immediate implication of a pdf is that we are now working on a continuous and non-binary (rather than good/not-good points) space, therefore transforming our $D(X, Y)$ into:

$$D(X, Y) = \int d(pdf X(\vec{x}), pdf Y(\vec{x}))d\vec{x}$$

Bhattcharya Distance

In order to compare the similarity between two estimated PDF, we have to define a measure of similarity, however this is not a trivial task either. The problem, namely, is that we are trying to transform a 2-dimensional information into a linear order, where we cannot compare the success rate of different methods by collating our results with an empirical distance measure. For now, we choose our similarity measure as Bhattcharya distance, where we
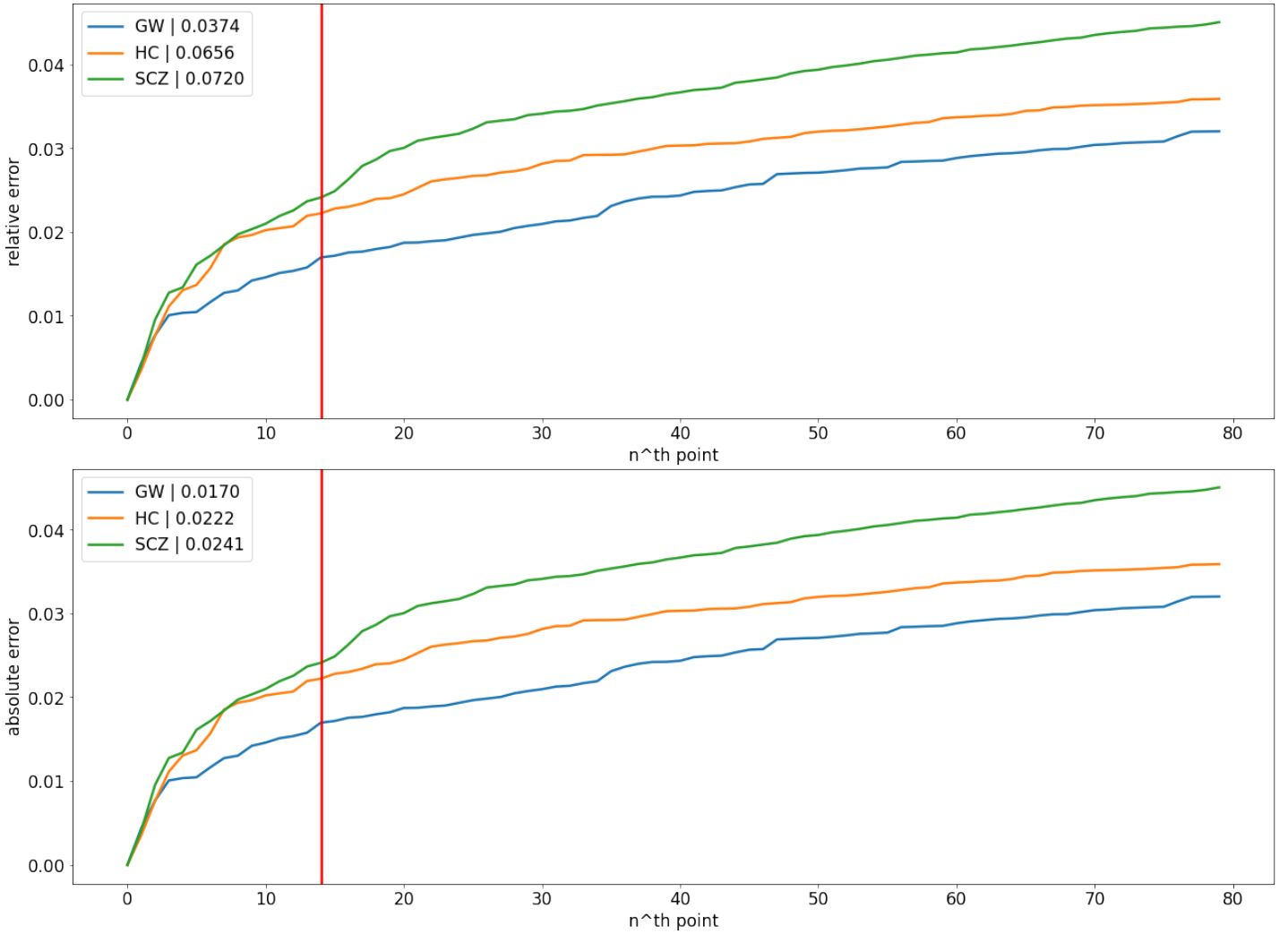
will be evaluating the agreement between our distance measure (thus also KDE) and the empirical data in the Sec.3.2.

Bhattcharya distance $D_B(p, q)$ [39] is defined as:

$$D_B(p, q) = -\ln(BC(p, q))$$

$$BC(p, q) = \int \sqrt{p(\vec{x}) \cdot q(\vec{x})} d\vec{x}$$

and numerically computed using `scipy.integrate.nquad` in the range $[-\infty, \infty] \times [-\infty, \infty]$.

Fig. 2.19: Relative and absolute differences of nth point to the best point

We have calculated the absolute and relative differences of nth point to the best point in the $simFC$-$empFC$ correlations and then averaged the values by data-set. Red vertical line indicates the 15th best point and the values on the legend shows the value of absolute/relative difference at 15th point w.r.t the data set.

Technische Universität Berlin
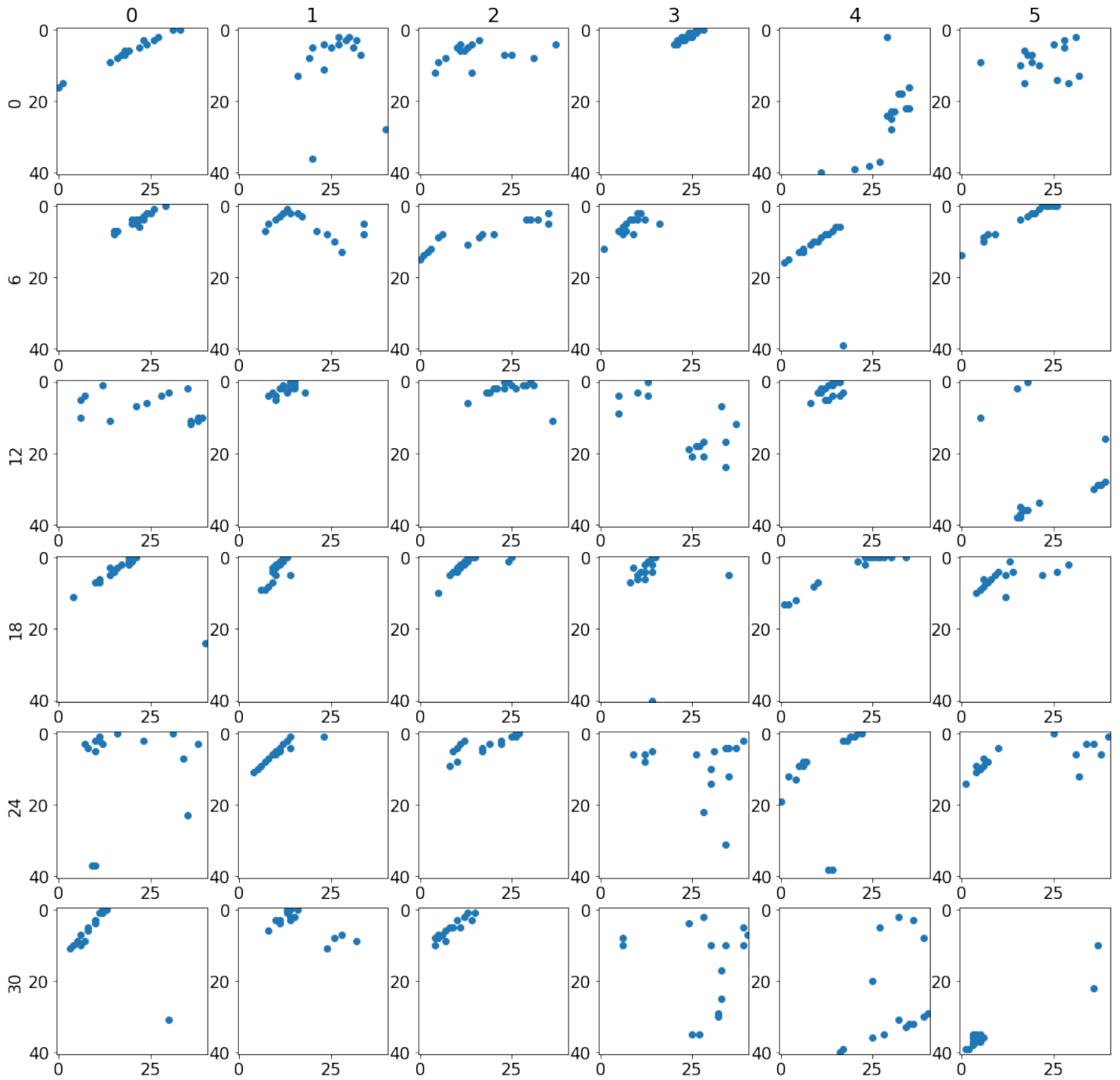
Fig. 2.20: Scatter plot of best 15 points of every individual to its own empFC

Individuals are numbered from left-to-right and up-to-bottom. Individual index can be calculated by $(row \times 6) + column$.
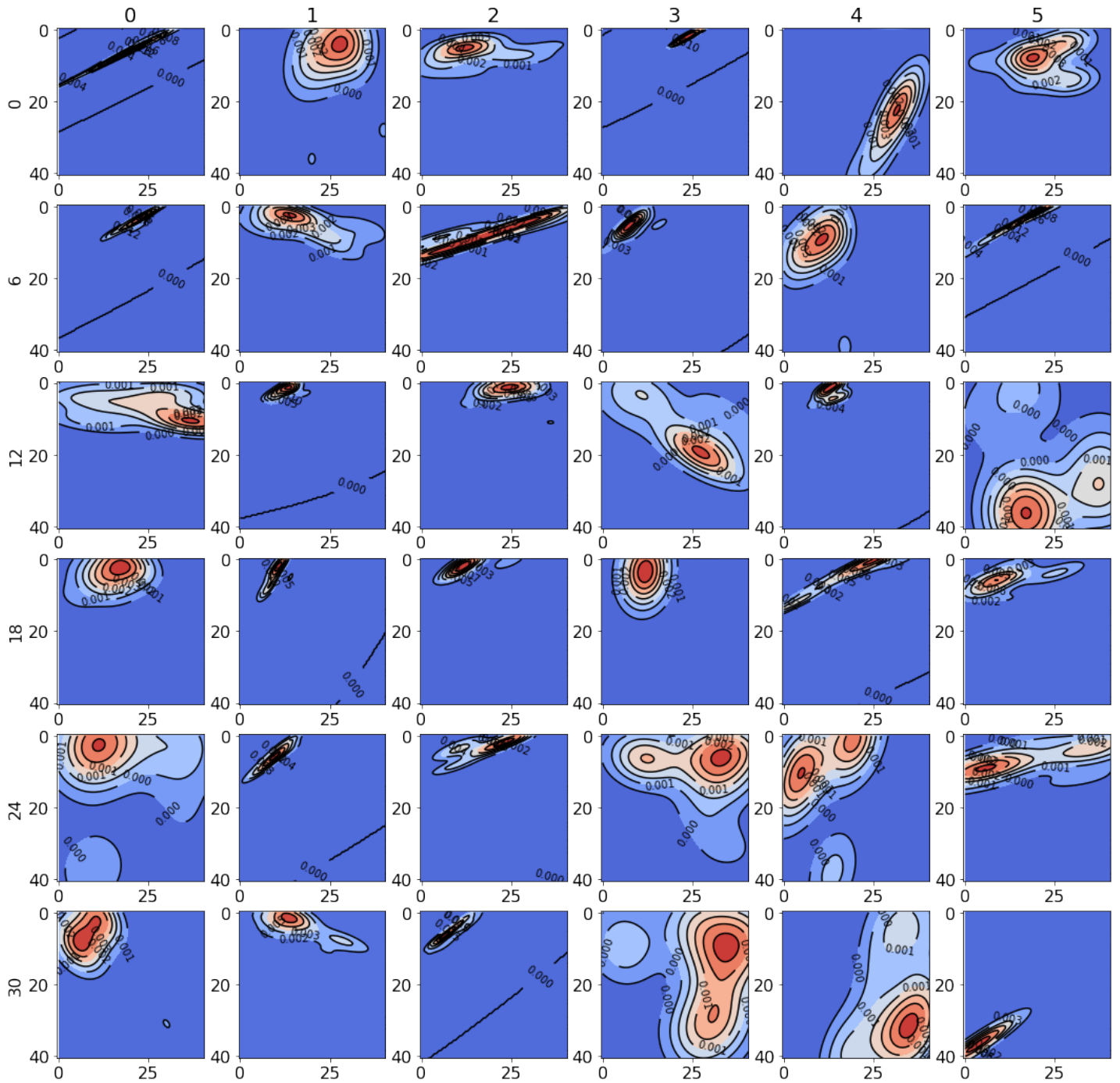
Fig. 2.21: Gaussian KDE of best 15 points of every individual to its own empFC

Individuals are numbered from left-to-right and up-to-bottom. Individual index can be calculated by $(row \times 6) + column$
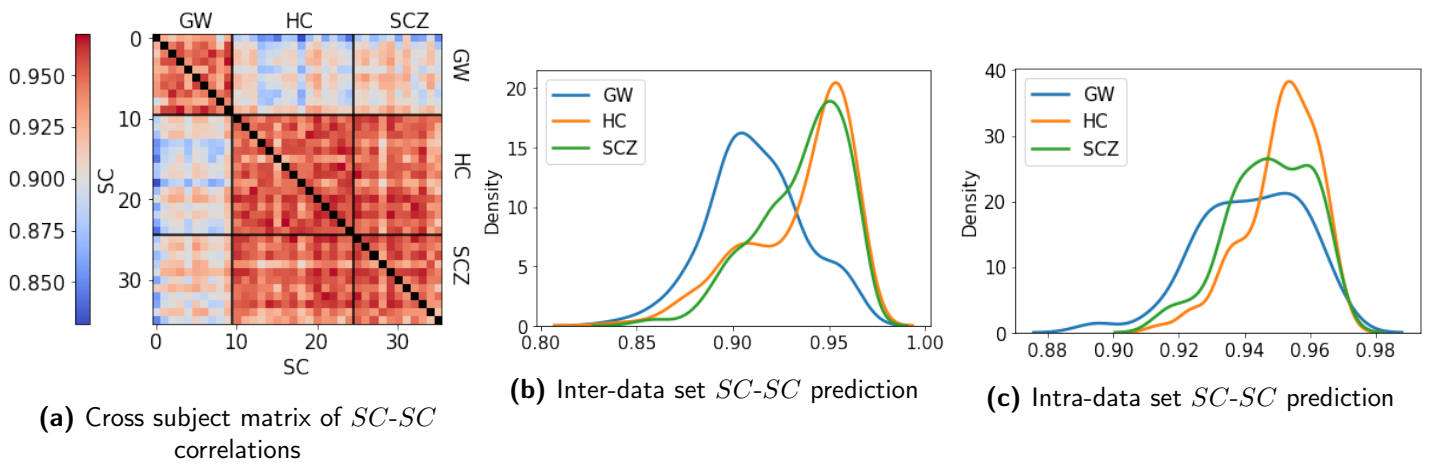
3. Results

In the result chapter, we will start with analyzing the empirical data in order to identify and demonstrate the differences among the data sets. Firstly, we will be discussing how does the SC matrices differ due to different imaging parameters and schizophrenia, then we will be examining how good can $empFC$s predict other $empFC$s in the same and different data sets. Lastly, we will try to explain how can we relate our observations from SC and $empFC$ to each other.

Secondly, we will be investigating the subject specificity of both $simFC$s and $simFCD$s, and the effects of both underlying SC and the compared $empFC/empFCD$ on the goodness of fit of our model. We will also be trying to relate our observations in simulated data to the empirical data. Later, in order to be able to find out how much does the underlying SC and our model selection effect the $simFC$, we will be investigating $simFC - SC$ and $simFC - simFC$ correlations.

For the last part, we will be examining the optimal working points of the FHN network and to what degree does the underlying SC determine the optimal parameter selection. We will also be interested in the parameter combinations where SC shapes the $simFC$ strongly, and the overall synchrony of both $BOLD$ signal and the FHN output using Kuramoto order parameters.

3.1. Emprical Data Analysis

3.1.1. SC-SC Correlation

(a) Cross subject matrix of SC-SC correlations

(b) Inter-data set SC-SC prediction

(c) Intra-data set SC-SC prediction

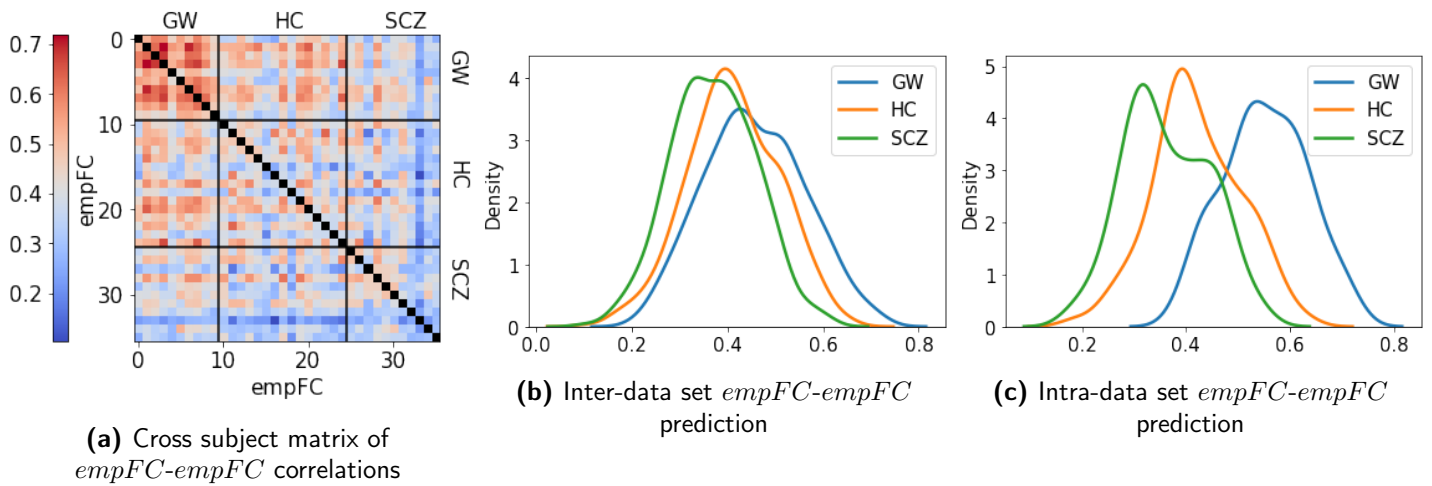**Fig. 3.1: (a)**: Cross subject matrix of SC-SC correlations, where entry i, j is the Pearson correlation coefficient of the SC matrices belonging to the individual i and j. **(b)**: plotted distributions rows/columns with respect to the data sets of the (symmetric) cross subject matrix. **(c)**: the distribution belonging to the SC-SC correlations of matrices from the same data set

As it can already clearly be seen Fig:3.1a, there are significant differences in the GW and other data sets, where SCZ and HC data sets are more similar to each other compared to GW data set. The reason, as explained in sec:2.1, is that these two data sets are acquired in a separate study and with different imaging parameters.

In order to evaluate the cross subject matrix numerically, we now plot the inter data set distributions (i.e the rows w.r.t the data sets, Fig:3.1b). We can clearly see that $SC\text{-}SC$ correlations of $HC\&SCZ$ data sets are more homogeneous compared to the GW data set ($HC\text{-}SCZ$ distributions KS-test p-value = 0.054 >0.05, D-statistics = 0.089). In order to observe the differences in the HC and SCZ data sets and to refine the effects of GW data set, we know plot the intra data set distributions of $SC\text{-}SC$ predictions (i.e 1st, 5th and 9st regions of the matrix, Fig:3.1c, we see there exists differences among all the data sets (all the KS-test p-values <0.01, and the D-statistics $\geq$0.225)
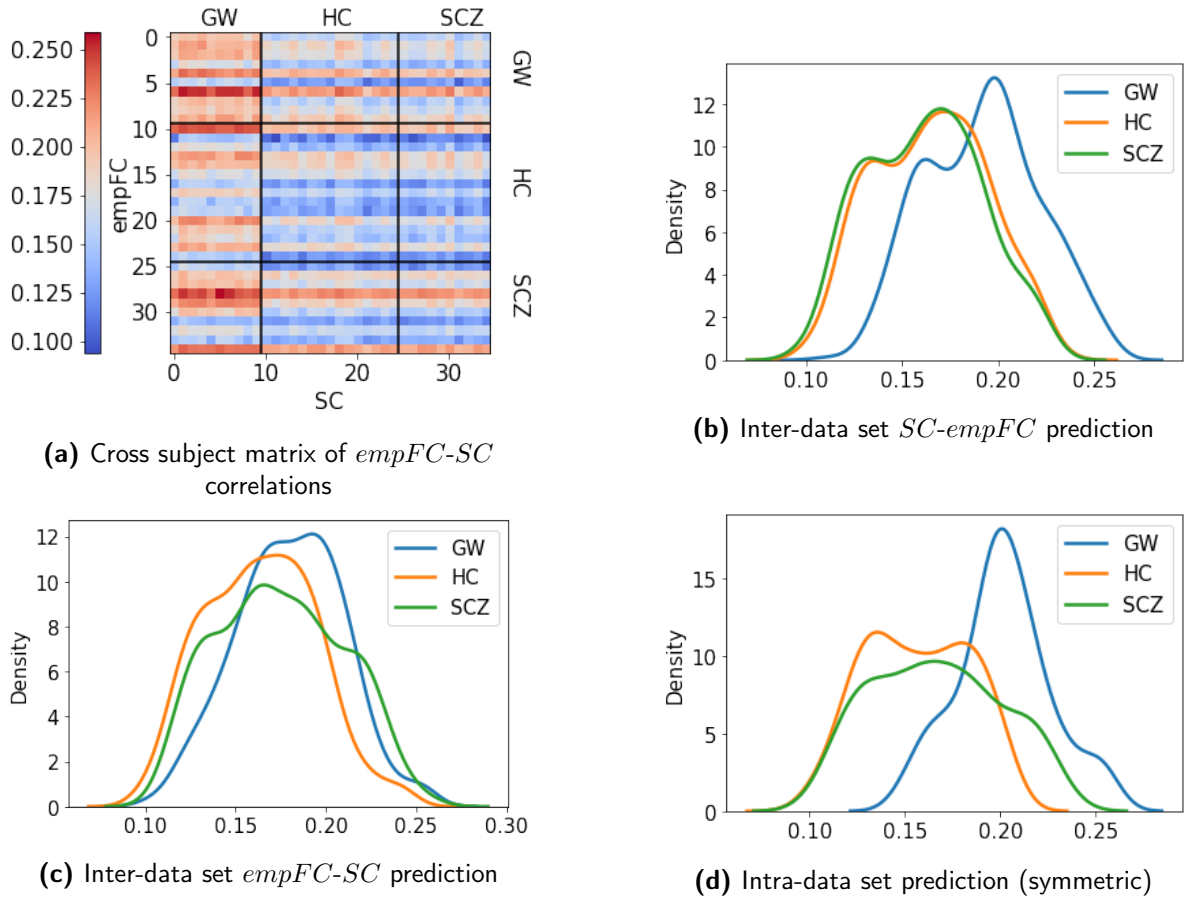
3.1.2. empFC-empFC Correlation

(a) Cross subject matrix of $empFC\text{-}empFC$ correlations

(b) Inter-data set $empFC\text{-}empFC$ prediction

(c) Intra-data set $empFC\text{-}empFC$ prediction

Fig. 3.2: (a): Cross subject matrix of $empFC\text{-}empFC$ correlations, where entry i, j is the Pearson correlation coefficient of the $empFC$ matrices belonging to the individual i and j. **(b)**: plotted distributions rows/columns with respect to the data sets of the (symmetric) cross subject matrix. **(c)**: the distribution belonging to the $empFC\text{-}empFC$ correlations of matrices from the same data set

We observe (Fig:3.2a) that $empFC\text{-}empFC$ correlations are less homogeneous than the $SC\text{-}SC$ predictions. We can already see that there are differences in the prediction power of $empFC\text{-}empFC$ matrices depending on the data set. When we plot the distributions of how good a data set can be predicted by all other data sets (i.e how good a data set can predict all other data sets (symmetric matrix), i.e rows or columns of the cross subject matrix, Fig:3.2b), we see that there is an order, s.t $GW > HC > SCZ$, and this effect is even stronger when we plot only intra-data set distributions (i.e 1st, 5th and 9st regions of the matrix, Fig:3.2c) (all KS-test p-values <0.01, all D-statistics$\geq$0.177 and visible shifts in the distributions)

3.1.3. empFC-SC Correlation

(a) Cross subject matrix of $empFC$-SC correlations

(b) Inter-data set SC-$empFC$ prediction

(c) Inter-data set $empFC$-SC prediction

(d) Intra-data set prediction (symmetric)

Fig. 3.3: (a): Cross subject matrix of $empFC$-SC correlations, where entry i, j is the Pearson correlation coefficient of the $empFC$ matrix belonging to the individual i and the SC matrix belonging to the individual j. **(b)**: plotted distributions of columns with respect to the data sets of the cross subject matrix. **(c)**: plotted distributions of rows with respect to the data sets of the cross subject matrix. **(d)**: the distribution belonging to the $empFC$-SC correlations of matrices from the same data set
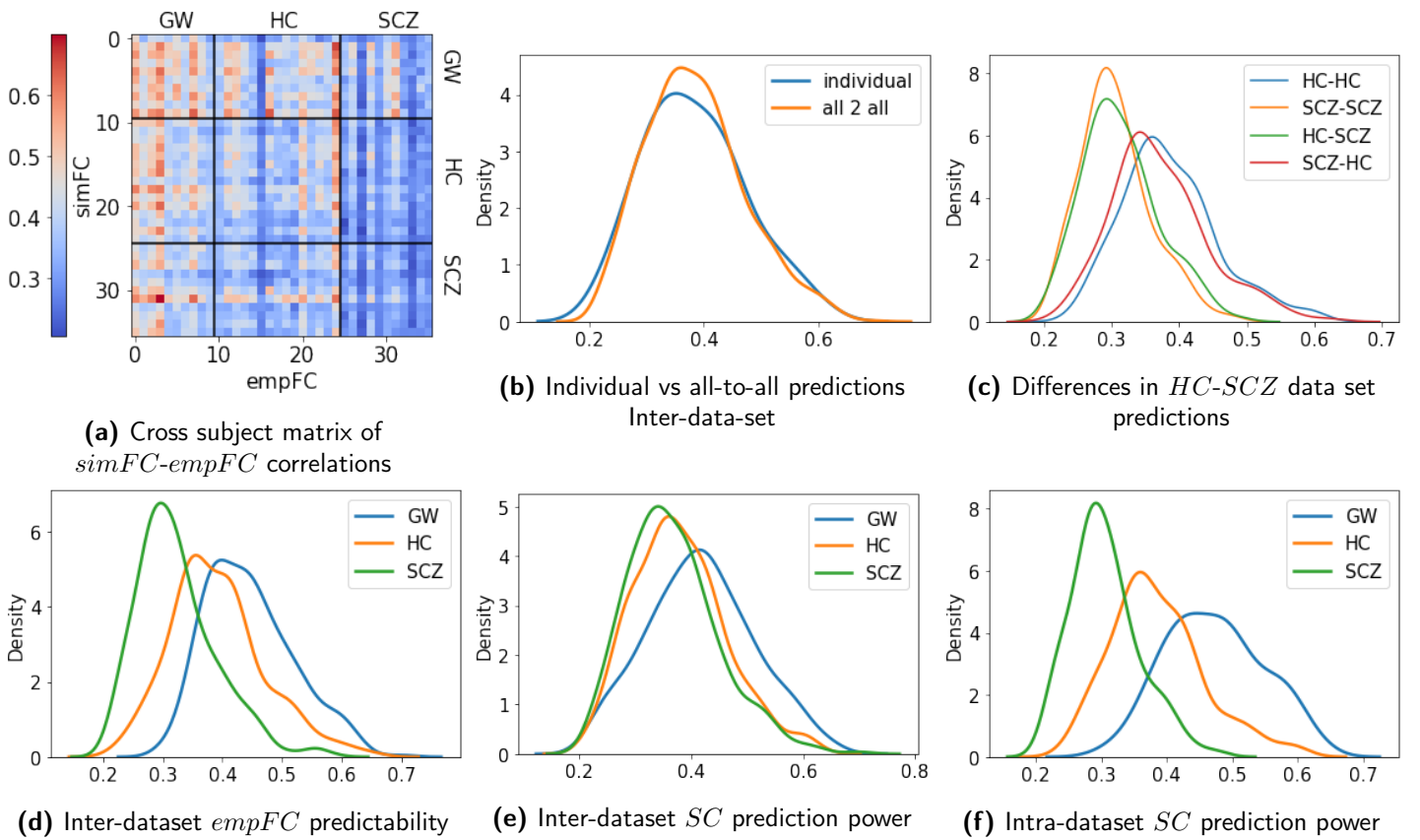
As a corollary of less homogeneous $empFC$-$empFC$ cross subject correlation compared to SC-SC correlation, we can already see that (the horizontal stripes in Fig:3.3a), there are no individual fits, rather some $empFC$s fit all of the SCs better. However, as Triebkorn [18] discussed, it should be further researched if the lack of individual fits are caused by an actual lack of variations in the SC or due to differences in the data acquisition process of SC and $empFC$.

When we investigate further the differences of data sets, we notice that SCs from GW data set are more powerful in terms of predicting all $empFC$s, where SCs from HC and SCZ data set have similar prediction power (for HC-SCZ: Fig:3.3b KS-test p-value = 0.231, D-statistics = 0.068 and Fig:3.3d KS-test p-value 0.03, D-statistics = 0.160). Given that GW data set has a better quality compared to the other two data sets, this might be one of the explanations for the better SC-$empFC$ predictions.

3.2. Simulated Data Analysis

We have conducted a 4 dimensional parameter space exploration on all of the 36 individuals, simulating the regional neural activity using the FHN model that takes the SC, LM and the parameters as an input, and then transforming the neural activity to the simulated $BOLD$ signals with the hemodynamic model [27]. We have later calculated $simFC$ and $simFCD$ matrices from the $simBOLD$ signal, and compared the simulated data against the empirical data. In this section, we will be investigating how were our simulations affected by the underlying SC, and if the simulation results have presented us a subject specific fit.

3.2.1. simFC-empFC Correlation

(a) Cross subject matrix of $simFC$-$empFC$ correlations

(b) Individual vs all-to-all predictions Inter-data-set

(c) Differences in HC-SCZ data set predictions

(d) Inter-dataset $empFC$ predictability

(e) Inter-dataset SC prediction power

(f) Intra-dataset SC prediction power

Fig. 3.4: (a): Cross subject matrix of $simFC$-$empFC$ correlations, where entry i, j is the Pearson correlation coefficient of the $simFC$ matrix belonging to the individual i and the $empFC$ matrix belonging to the individual j. **(b)**: Distributions of the diagonal (individual predictions where $simFC$ and $empFC$ belongs to the same individual) and non-diagonal (entries where $simFC$ and $empFC$ belongs to different individuals) entries of the cross subject matrix. **(c)**: The distributions of 5th, 6th, 8th and 9th regions, where the first data set in the legend denotes the SC used and the second denotes the $empFC$. **(d)**: plotted distributions of columns with respect to the data sets of the cross subject matrix. **(e)**: plotted distributions of rows with respect to the data sets of the cross subject matrix. **(f)**: the distribution belonging to the $simFC$-$empFC$ correlations of matrices from the same data set

Subject Specificity

In order to evaluate subject specificity of $simFC$s (as in [18]), we plot (Fig:**??**) the distribution of subject's individual predictions (diagonal entries of the cross subject matrix) and subject's prediction of all other $empFC$s (non diagonal entries). Regardless of data-set (both inter- and intra-data set distributions), we see that, individual predictions are no better than all-to-all predictions (for inter data set: KS-test p-value = 0.949, D-statistics = 0.084 and for intra data set: all KS-test p-values $\geq$0.432, all D-statistics $\leq$0.278). As discussed in [18] and section 3.1, this could be a result of different level of imaging quality in SC and $empFC$ data, a lack of variation in SC or a fundamental consequence of our model.
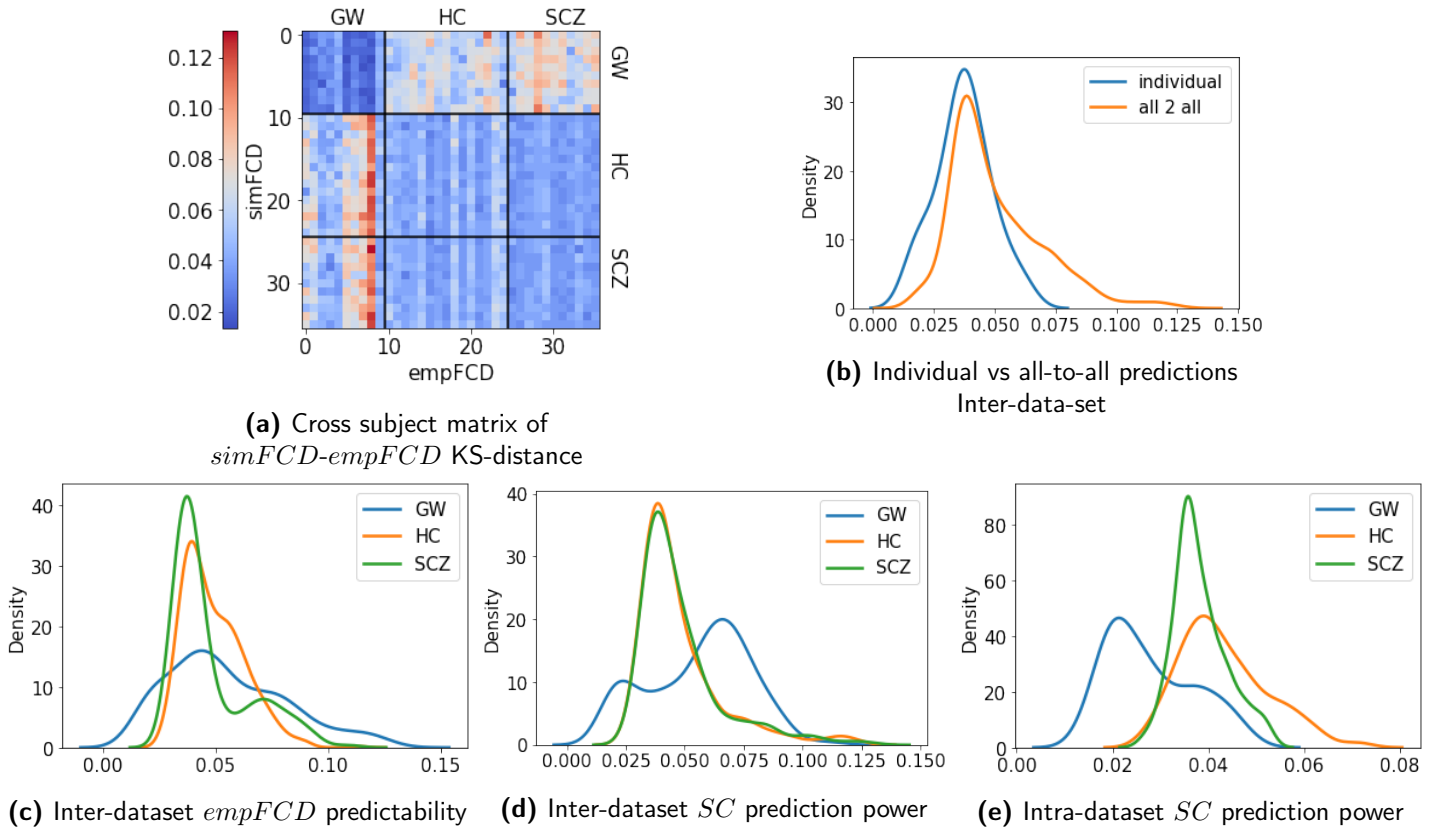
Inter-data set Differences

In order to understand effects of our model selection, we plot inter-dataset $empFC$ predictability (3.4d), inter-dataset SC prediction power (3.4e) and intra-dataset SC prediction power (or $empFC$ predictability by symmetry 3.4f).

Only similar distribution in the figures above is $HC\text{-}SCZ$ inter-dataset SC prediction power (KS-Test p-value = 0.037, D-statistics = 0.092 and for SC that belongs to $HC\&SCZ$ prediction of $empFC$s belonging to GW,HC and SCZ (see appendix:A.2) p-values: 0.130, 0.011, 0.347, D-statistics: 0.144, 0.162, 0.109). These results coincide with our observations in the empirical data analysis (sec: 3.1) both for SC and FC side, i.e:

- SCs that belong to the HC and SCZ data-set are more similar to each other than GW data-set, however have a lower imaging quality, therefore their prediction powers are similar but less powerful than GW data-set (see 3.1.1)

- There is an order according to data-set in predictability of $empFC$ ($GW > HC > SCZ$), where our simulated results agree with this order regardless of which SC is used (see 3.1.2 and appendix:A.2)

- When we compare only the $HC\text{-}SCZ$ data sets, that are acquired in the same study with the same imaging parameters, we still see that $empFC$s that belong to the HC data set can be predicted better than the $empFC$s that belong to the SCZ data set, where the used SC doesn't effect the prediction power significantly ($HC-HC\text{-}SCZ-HC$: KS-test p-value=0.115, D-statistic=0.162, $HC-SCZ\text{-}SCZ-SCZ$: KS-test p-value=0.347, D-statistic=0.109, and for all other combinations p-value$\leq$0.01)

3.2.2. simFCD-empFCD KS Distance

Here in this section, we aim to investigate the $simFCD$ matrices, that represents the change in resting state functional connectivity over time [33] and relevant in the schizophrenia research [34]. We again plot cross subject matrix of KS-test D-value (as a measure of distance), and distribution of diagonal and non-diagonal entries of cross subject matrix.

(a) Cross subject matrix of
$simFCD\text{-}empFCD$ KS-distance

(b) Individual vs all-to-all predictions
Inter-data-set

(c) Inter-dataset $empFCD$ predictability

(d) Inter-dataset SC prediction power

(e) Intra-dataset SC prediction power

Fig. 3.5: (a): Cross subject matrix of $simFCD\text{-}empFCD$, where entry i, j is the KS-test D-statistic of the $simFCD$ matrix belonging to the individual i and the $empFCD$ matrix belonging to the individual j. **(b)**: Distributions of the diagonal (individual predictions where $simFCD$ and $empFCD$ belongs to the same individual) and non-diagonal (entries where $simFCD$ and $empFCD$ belongs to different individuals) entries of the cross subject matrix. **(c)**: plotted distributions of columns with respect to the data sets of the cross subject matrix. **(d)**: plotted distributions of rows with respect to the data sets of the cross subject matrix. **(e)**: the distribution belonging to the $simFCD\text{-}empFCD$ correlations of matrices from the same data set

Subject Specificity

The failure of the GW data-set in predicting $empFCD$ belonging to $HC\&SCZ$ (and vice-versa) is visually notable already in the Fig:3.5a. As a consequence, we see that individual inter-data set predictions are more homogeneous and slightly better than all-to-all predictions (KS-test p-value <0.01, D-statistics = 0.287). However when we plot intra-data set individual vs all-to-all predictions (including regions 5,6,8,9 together, i.e inter-data set for only the HC&SCZ, see:2.3.5 and A.2), we notice that Fig:3.5b is misleading, and the individual predictions are no better than all-to-all predictions (KS-test p-values: 0.815, 0.985, 0.810, 1.000 and D-statistics: 0.200, 0.114, 0.191, 0.066).

Inter-dataset Differences

In order to comprehend the effects of SC, $empFCD$ and different image qualities, we now plot inter-data set $empFCD$ predictability, inter-data set SC prediction power and intra-dataset SC prediction power (as well as their specific combinations in appendix A.2). We

are again able to replicate some of our observations from previous sections, as follows:

- from Fig:3.5c and Fig:3.5e, we see that depending on the data set used, the predictability of $empFCD$ vary. However on the contrary to FC results, predictability of SCZ is slightly better than HC (all KS-Test p-values <0.01 and D-statistics ≥0.210, also see A.2).

- in Fig:3.5d, and specific plots from SC to all $empFCS$ (see see A.2), we deduce that SC's from $HC\&SCZ$ data sets have similar prediction power, implying how strongly SC shapes $simFCD$ (KS-test p-value = 0.980 and D-statistic = 0.030).

- Lastly, we notice the failure of SC from GW to predict $empFCD$ from $HC\&SCZ$ (and vice-versa, given that they are both data from healthy subjects), it shows us how much effect the imaging quality has.

3.2.3. simFC-SC Correlation

Following the previous results, in an effort to understand the effects of SC on the simulation results, we now explore $simFC$-SC correlations. Therefore, we plot cross subject matrix of $simFC$-SC correlation, individual vs all-to-all prediction of inter-data set (diagonal and non-diagonal entries), and a scatter plot where X-axis is $simFC$-SC correlation and Y-axis is SC-SC correlation of every individual combination (36×36 as in [18])

(a) Cross subject matrix of $simFC$-SC correlations

(b) Individual vs all-to-all predictions Inter-data set

(c) Intra-data set scatter plot
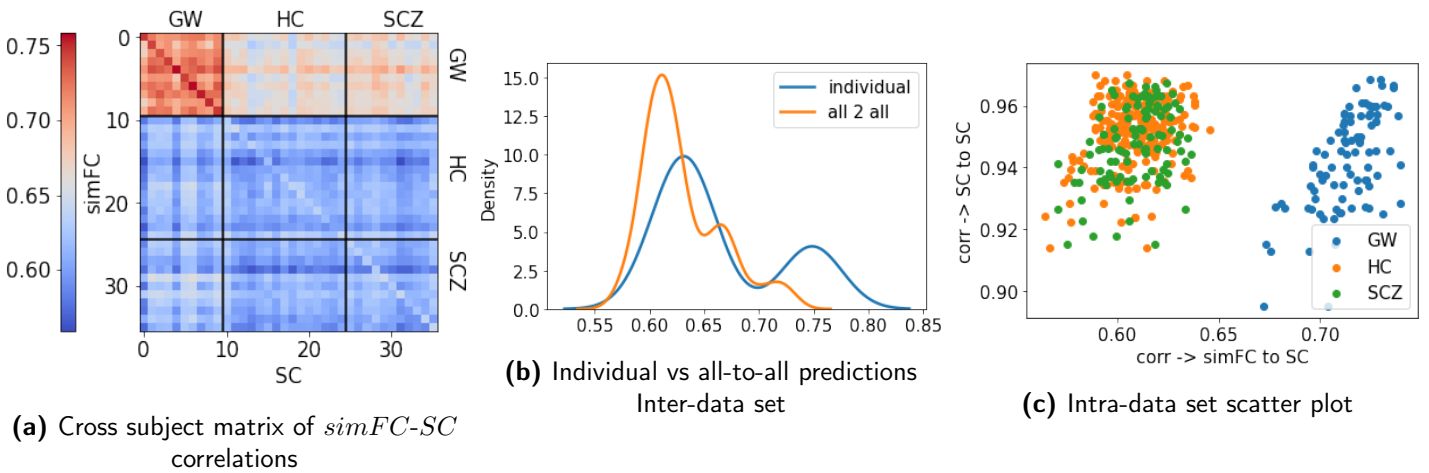
Fig. 3.6: (a): Cross subject matrix of $simFC$-SC correlations, where entry i, j is the Pearson correlation coefficient of the $simFC$ matrix belonging to the individual i and the SC matrix belonging to the individual j. **(b)**: Distributions of the diagonal (individual predictions where $simFC$ and SC belongs to the same individual) and non-diagonal (entries where $simFC$ and SC belongs to different individuals) entries of the cross subject matrix. **(c)**: X-axis contains the entries from cross subject matrix of $simFC$-SC, where both $simFC$ and SC belongs to the individuals from the same data set and y-axis is the corresponding entries from cross subject matrix of SC-SC correlations (without the diagonal, where points are colored w.r.t data set.

The diagonal entries in the Fig. 3.6a already indicates that individual predictions are better than all-to-all predictions. Both in Fig.3.6b and intra-data set plots (see A.2), we see that for

all data sets individual predictions are significantly better than all-to-all predictions (KS-Test p-values <0.01 and all D-statistics ≥0.403).

Moreover, when we scatter plot (Fig. 3.6c) the relation between SC-SC correlation and $simFC$-SC correlation in intra-data set points, we see that for GW data set there is a strong linear relationship (correlation = 0.618, p-value <0.01) compared to the other two data sets (0.256 for HC and 0.368 for SCZ with all p-values <0.01).

Thus, similar to [18], we argue that, the input SC can have a significant effect on the $simFC$ for some parameter combinations, but this doesn't have to be true for optimal working points of the network with respect to the $empFC$. However it can be further investigated, how does this effect depends on the imaging quality in the evolution of the model, given that SCs from SCZ&HC are sparser and of poor quality and can be predicted worse by $simFC$ compared to the GW data-set.

3.2.4. simFC-simFC Correlation

Similar to the argument in the previous section (3.2.3), we create cross subject matrix of $simFC$-$simFC$, a scatter plot where X-axis is $simFC$-$simFC$ correlation and Y-axis is SC-SC correlation of every individual combination.

(a) Cross subject matrix of $simFC$-$simFC$ **(b)** Inter data set scatter plot
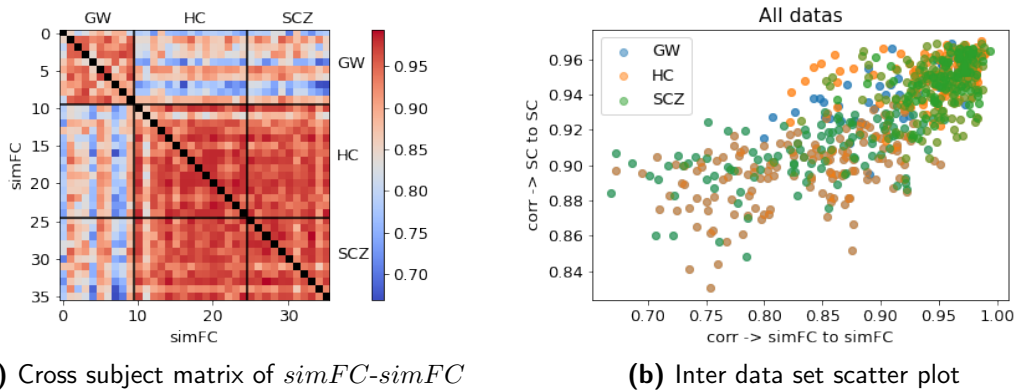
Fig. 3.7: (a): Cross subject matrix of $simFC$-$simFC$ correlations, where entry i, j is the Pearson correlation coefficient of the $simFC$ matrix belonging to the individual i and the $simFC$ matrix belonging to the individual j.**(b)**: X-axis contains all of the entries from cross subject matrix of $simFC$-$simFC$, and y-axis is the corresponding entries from cross subject matrix of SC-SC correlations (without the diagonal), where points are colored w.r.t data set.

Inter-data set differences can already be clearly seen at Fig.3.7a. Furthermore, the Fig.3.7b shows us that SC-SC correlations are strongly correlated with $simFC$-$simFC$ correlations (All points correlation: 0.771, intra-data set correlations in order GW,HC,SCZ: 0.684, 0.310, 0.326, all p-values <0.01), implying that there are some parameter combinations that are strongly shaped by SC. Even though these observations are similar to the observations in section 3.2.3, in order to understand the effects of FHN network and the possible cause of the similarity, we still need to analyze the parameter combinations in the next section.
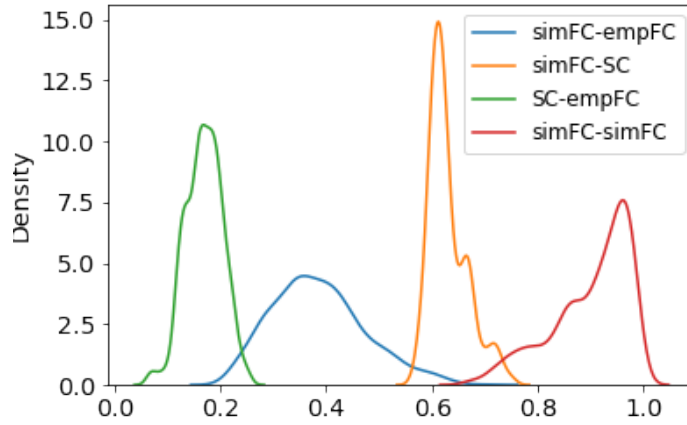
Fig. 3.8: The distributions corresponding to the cross subject matrices of $simFC\text{-}empFC$, $simFC\text{-}SC$, $SC\text{-}empFC$ and $simFC\text{-}simFC$

In the analysis of the simulated data, we have concluded that due to lack of variations in the SC matrices, the FHN model combined with the hemodynamic model cannot make individual predictions better than all-to-all predictions, yet for the $simFC\text{-}empFC$ predictions, not only it was able to capture the order in the predictability of $empFC$s depending on the data set, but also it was able to make better predictions compared to $SC\text{-}empFC$ predictions (Fig.3.8). We have also shown that for some parameter combinations, the $simFC$ are able to predict each other and the underlying SC better than $empFC$. We will be investigating the parameter combinations that leads to good $simFC\text{-}empFC$, $simFC\text{-}SC$ and $simFC\text{-}simFC$ in the next section.

3.3. Parameter Space Analysis

3.3.1. simFC-empFC Parameter Space
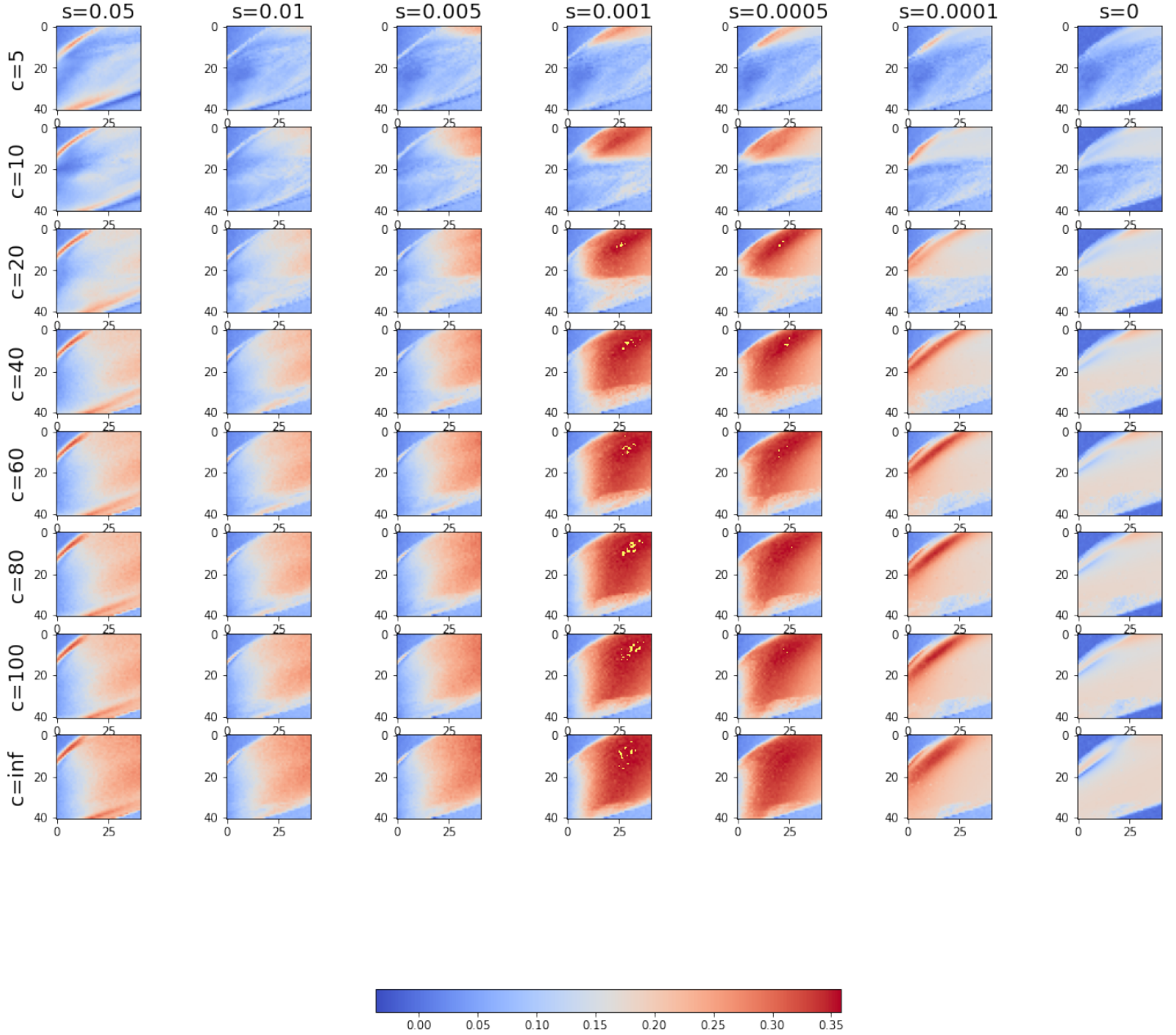
Fig. 3.9: Averaged $simFC\text{-}empFC$ parameter space, both $simFC$s and $empFC$s are from the GW data set, where the axis values of a single image gives the c and σ values, and for every sub figure the vertical axis gives the I_{ext} index, and the horizontal axis gives the K index. the 100 best points are shown with yellow.

Since this is an averaged parameter space plot, individual variances are lost, however some of the interesting regions should be identified for further discussion in the result section:

1. Left-upper and right-lower corners: these low correlation regions, with low I/K or high I/K parameters, exist regardless of the used SC, and the FHN network doesn't function properly due to either low or high level of activity in these regions. They can be identified by either Kuramoto order parameter of $simBOLD$ or the FHN output.

2. Just at the edge of previous regions and the elliptical region in the middle (can clearly be seen at s=0.05), there is one of the interesting regions. This region exists also regardless of used SC.

3. And lastly, the high correlation line from (I=20,K=0) to (I=0,K=25) (can clearly be seen at s=0.0001)

It is important to mention that bifurcation points for the uncoupled FHN node is at $I = 0.7$ (index 20 in the vertical axis) and at $I = 1.35$ (would be index 44 in the vertical axis if it was evaluated as well), which are very close to the identified 2nd and 3rd regions for low K (horizontal axis) values, and I_{ext} values decreases as K increases.
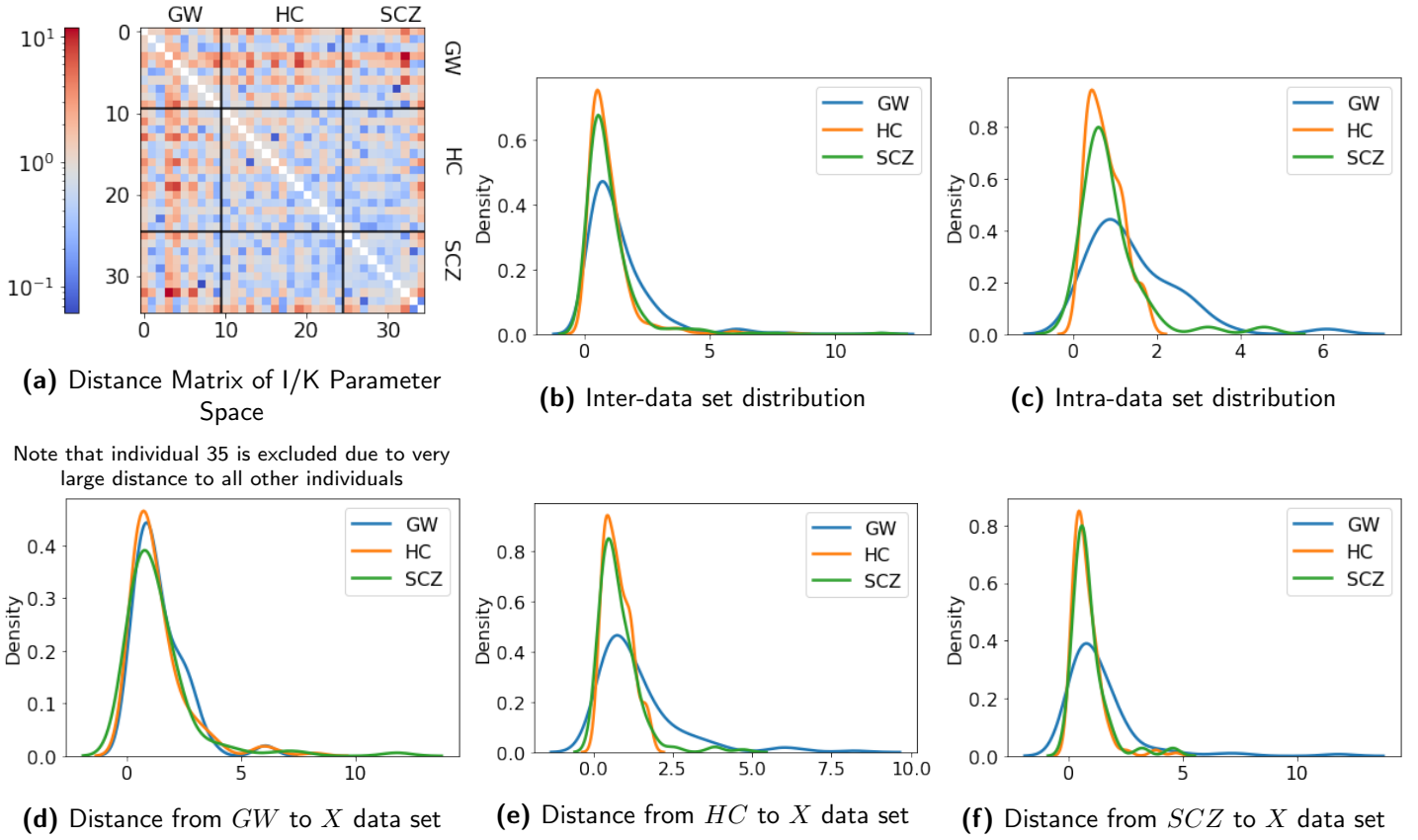
Optimal Working Points of individual predictions: I/K Space

Here, we plot the distance matrix of individual predictions in log-scale (i.e SC and $empFC$ belong to the same individual) and relevant distributions. Visually, we can easily see that GW data set is less homogeneous in terms of optimal working points compared to the two other data sets, this can also be confirmed from the distributions (HC-SCZ inter-data set and intra-data set KS-test p-value: 0.674, 0.218 and D-statistics: 0.050, 0.130).

To be able to go into more detail, we also plot the distribution of distances from specific data set to all other data sets (Data set column of Fig:3.10a).

- Distributions from GW to all other data sets are similar (all KS-test p-values $\geq$0.101 and all D-statistics $\leq$0.173 , Fig:3.10d)

- Distributions from HC to HC&SCZ are similar (KS-test p-value = 0.405 and D-statistic = 0.093, Fig:3.10e)

- Distributions from SCZ to HC&SCZ are similar (KS-test p-value = 0.079 and D-statistic = 0.167, Fig:3.10f)

When we go through the averaged $simFC$-$empFC$ parameter-space plots (A.2), we see that for HC and SCZ data sets the optimum working points are more homogeneous compared to GW data set. For both HC and SCZ data set, optimum working points found on the 2nd and 3rd regions (as we have defined above), where for GW data set they can be found as well in the elliptical region in the middle. This observation, even though a better understanding of underlying functionality is needed, is consistent with the interpretation of Fig. 3.10b & 3.10c, where we see a wider distribution for the GW data.

(a) Distance Matrix of I/K Parameter Space

Note that individual 35 is excluded due to very large distance to all other individuals

(b) Inter-data set distribution

(c) Intra-data set distribution

(d) Distance from GW to X data set

(e) Distance from HC to X data set

(f) Distance from SCZ to X data set

Fig. 3.10: (a): The entry i, j contains the Bhattacharya distance between estimated density of optimal working points (only I/K) belonging to the $simFC_i$-$empFC_i$ correlations and the $simFC_j$-$empFC_j$ correlations. **(b)**: plotted distributions of rows/columns with respect to the data sets of the (symmetric) cross subject matrix. **(c,d,e)**: plotted distributions of the columns with respect to the data sets for a single row of the cross subject matrix

Another important observation from the averaged $simFC$-$empFC$ parameter-space plots, is that the input SC matrix shapes the optimal working points (and parameter-space) more effectively than the $empFC$.

Optimal Working Points: c/σ Space

When we plot distribution of highest 15 $simFC$-$empFC$ correlations of every individual (SC and $empFC$ belong to the same individual) depending on the c and σ values, we notice that for $c > 10$, the selection of the parameter c is less important compared to the other parameters as discussed in [18] (all KS-test p-values ≥ 0.375 and all D-statistics ≤ 0.055). Yet this is not true for σ, where the optimum value depends on the data set (see A.2).

(a) c **(b)** σ
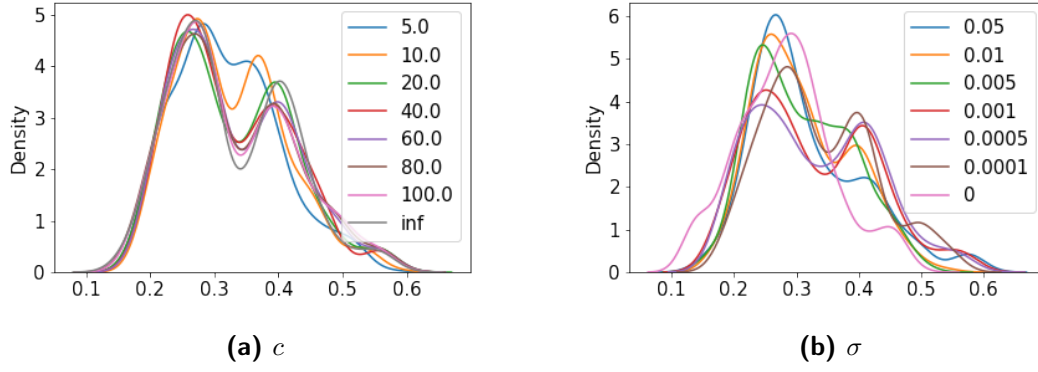
Fig. 3.11: For varying **(a)** c and **(b)** σ values, we have plotted the distribution of 15 best individual $simFC$-$empFC$ (i.e $simFC$ and $empFC$ belongs to the same individual) correlation values, (i.e 15×36 data points per distribution)

3.3.2. Effects of underlying SC

$simFC$-SC **Parameter Space**

As we have discussed in 3.2.3, we know that there exists some parameter combination, where $simFC$ is heavily shaped by the SC matrix. When we analyze the parameter space of $simFC$-SC correlations as we did previously in the 3.3.1 (see A.2 for related plots), we observe that the optimum working points are densely clustered in some regions, where we find almost all of 15 best correlation points in combination of low I_{ext}, high K, high σ and $40 \leq c \leq 80$ ranges. Even though high K and low I_{ext} values intuitively makes sense, we lack the necessary understanding of the inner dynamics to make a statement about why this is the case.

$simFC$-$simFC$ **Parameter Space**

Another metric that is highly affected by SC matrix are $simFC$-$simFC$ correlation values. To test if this phenomenon is related to $simFC$-SC case, we use a similar approach as previously, however since there are no individual-to-individual values, we use averaged (both for inter- and intra-data set, see A.2) matrices. We conclude that, the optimum working points are again very homogeneous however dependent on the SC matrix used. For GW data set, we find high correlation values in the edges of the elliptical region in the middle (2nd region as identified in the beginning of section) and $\sigma = 0.05$, and for the other data sets, at the lower points of the 3rd line with $\sigma = 0$.

3.3.3. Dynamics of the FHN model

In order to be able to understand how does the FHN model and the $empFC$ fit relates, we have tried to understand the dynamics of the FHN model, by not only analyzing the synchrony of both the FHN output and the $simBOLD$ signal, but also investigating the

frequency and the amplitude of the FHN oscillations.

Kuramoto Order Parameter of $simBOLD$ and FHN output
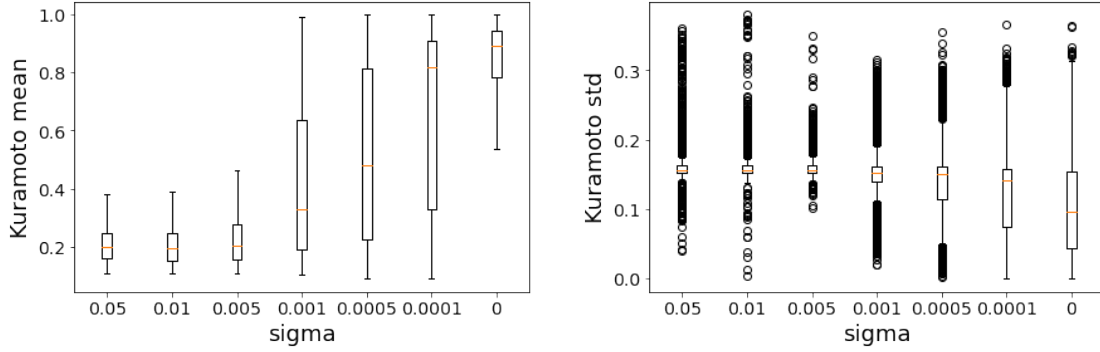
Fig. 3.12: Box plot of **(a)** mean of Kuramoto order parameter without outliers and **(b)** standard deviation of Kuramoto order parameter with outliers of all individuals (averaged) depending on the σ value

Even though we cannot directly relate synchrony (mean) and meta-stability (standard deviation) to the correlation of $simFC$-$empFC$, there are interesting overlaps independent of data set that should be mentioned. Firstly, we notice that both mean (inversely) and standard deviation (directly) of the Kuramoto order parameter is proportional to the σ value, where we don't see this relationship for the Kuramoto order parameter of the FHN output (see A.2), and this is likely to be caused by sensitivity of hemodynamic model to the noise in the scaled FHN output. For $c \leq 20$, where we see worse $empFC$ fits, we also see that, high syncrony is scarce. Furthermore at both of the interesting regions (identified in 3.3.1) that are related to high $simFC$-$simFC$ and $simFC$-$empFC$ correlation, we see maximum mean and minimum std of Kuramoto at the line 3 for $\sigma = 0$ and high values of c, and at the edge regions (identified as 2) we see high mean and high std of Kuramoto order parameter (see A.2)

Kuramoto order parameter of FHN output is less interesting compared to the Kuramoto order parameter of the $simBOLD$ and mean values are mostly ≥ 0.9, however it shouldn't be ignored, that only attention-worth regions regardless of data set with low mean (~ 0.5) and high std are the edge regions.

$maxbold$

In order to understand the effects of $maxbold$ parameter and also to evaluate how does the amplitude information in the FHN output translates into the $simBOLD$ signal, we have conducted a full grid search for $maxbold$ values in $[noscaling, 10, 20, 40, 60, 80, 100]$, with all 41 I_{ext} and K values, all $c \geq 20$ values and all $\sigma \geq 10^{-4}$ values using the matrix 3 (in the GW data-set), and 3 narrow grid searches for every fourth I_{ext} and K parameters and the rest of the parameters were the same as the full grid search for matrices 1 (GW), 12 (HC) and 32

(SCZ). Then we have calculated correlation of $simFC$ matrices for every combination of $maxbold$ keeping all of the other parameters same. We have also tried scaling the FHN output node-wise, i.e we have scaled every node individually from $[min\,of\,the\,node, max\,of\,the\,node]$ to $[0, maxbold]$ as opposed to scaling every node from the minimum and maximum of all nodes to $[0, maxbold]$ (see 2.2.3), and calculated correlation of $simFC$ outputs.

We have observed that for $maxbold$ values ≥ 40, regardless of the other parameters (i.e I_{ext}, K, c, σ), $simFC$-$simFC$ correlations are ≥ 0.99 for at least $\%94$ of parameter space, and ≥ 0.95 for at least $\%99.6$ of the parameter space, and similarly (also as a result of the previous observation) correlation between the node-wise scaling of the FHN output and usual scaling was ≥ 0.99 for $\%99.1$ of the parameter combinations.

For the rest of the $maxbold$ values except $= 20$, including values ≥ 40, the effect of $maxbold$ was very dependent on the σ values, where for $\sigma \geq 0.005$ at least $\%95$ of the parameter space had a correlation value ≥ 0.95 (except the lower edge of the middle elliptical region, 2nd region as identified before). Lastly and most interestingly, for $\sigma < 0.005$ we have seen the smallest correlation values at the 3rd line (as identified before) that was pinpointed as one of the high correlation region. However, these results don't necessarily have an implication on the relationship between the $maxbold$ parameter and the correlation of $simFC$-$empFC$, but can only give an intuition on the effects of the $maxbold$ parameter.

A sample of the FHN output in different time scales, the original $simBOLD$ and down-sampled $simBOLD$ can be found on the next page.
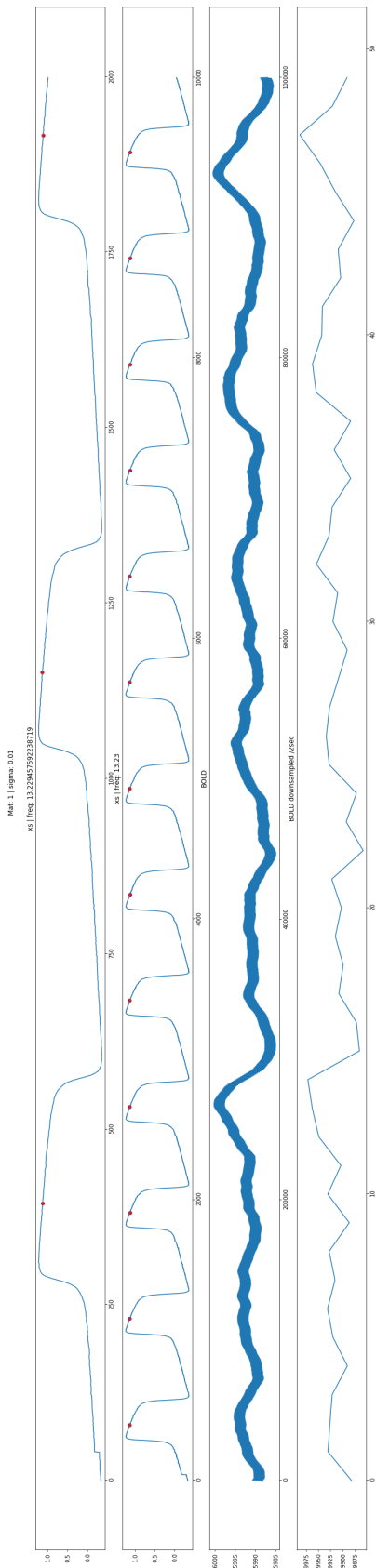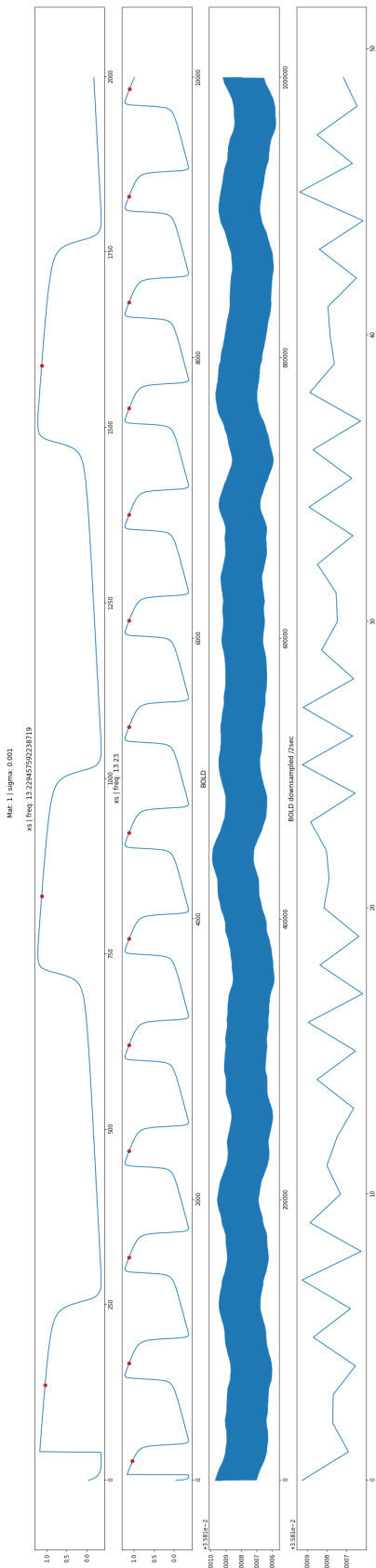
Fig. 3.13: Sample of the FHN output with σ **(a)**=0.01 and **(b)**=0.001, where the first plot is the FHN output from t=0 to t=2000 (200ms), second plot is the same FHN output for 500ms, the third plot is the original $simBOLD$ in 50s and the forth is the down-sampled $simBOLD$ for 50s

4. Discussions

In this study, we have employed a modeling approach using a derivation of the FitzHugh-Nagumo model and the hemodynamic model in order to simulate individual resting state functional connectivity from individual structural connectivity. We have conducted a parameter space exploration on the 4 parameters (I_{ext}, K, c and σ) of the FHN model, to get a good picture of optimal working points and to answer the question how do schizophrenia and different imaging qualities affect subject specificity, the goodness of $simFC$-$empFC$ fit depending on the parameters and if the optimal working points of the FHN network changes depending on the selected SC and/or $empFC$.

We have used SC and $empFC$ acquired using DTI and fMRI from 36 individuals (11 with schizophrenia, 15 healthy control subjects with the same imaging parameters used for the schizophrenia patients, and 10 more healthy control subjects acquired in a different study with different imaging parameters), and simulated for 94136 different parameter combination (a parameter that controls the bifurcation: I_{ext}, the global coupling: K, the conduction velocity: c and the standard deviation of the Gaussian noise: σ). Then we have compared the $simFC$ and $simFCD$ (calculated using the $simBOLD$) to the $empFC$ and $empFCD$.

We have previously tried to evaluate the effect of the simulation duration on the $simFC$-$empFC$ correlation, however due to extreme computational resources needed, it was not plausible to employ a similar grid search method here. Thus, we have explored a couple of different points selected with varying σ values, and we have observed that with the increasing duration the $simFC$-$empFC$ correlation increases while the noise in $simFC$-$empFC$ decreases (see Fig.4.1). However, this effect depends mostly on the selected σ values, where for $\sigma = 0$, we see rather a deterministic network. However the effects of duration become insignificant after 150000ms, thus we believe that the differences in the simulation differences depending on the data set don't have a significant effect on the $simFC$-$empFC$ correlations. However, we would most likely expect the duration to be more important for the $simFCD$-$empFCD$ where the change in functional connectivity over time matters, therefore we have selected our simulation duration regarding the duration of the empirical BOLD signal.

The correlation of empirical SCs among subjects were already much more homogeneous compared to the $empFC$, however there existed differences in SC's of the GW data set and other data sets, possibly indicating the effects of the different imaging parameters. However for the $empFC$ correlations we didn't see a similar difference between data sets, but rather $empFC$s from GW data set could be predicted better by all $empFC$s and SCs regardless of the data set, and $empFC$s from HC data set could be predicted better compared to SCZ data set by all other $empFC$s.

In accordance with the empirical data, we have observed the same order for the prediction power of simulated FC, where regardless of the $simFC$ used, $empFC$s from the GW data set could be predicted best, and $empFC$s from the SCZ data set were predicted worst. Since both SC and $empFC$ of the HC and SCZ data acquired in the same research with the same imaging parameters and with similar demographics except the psychiatric health condition of
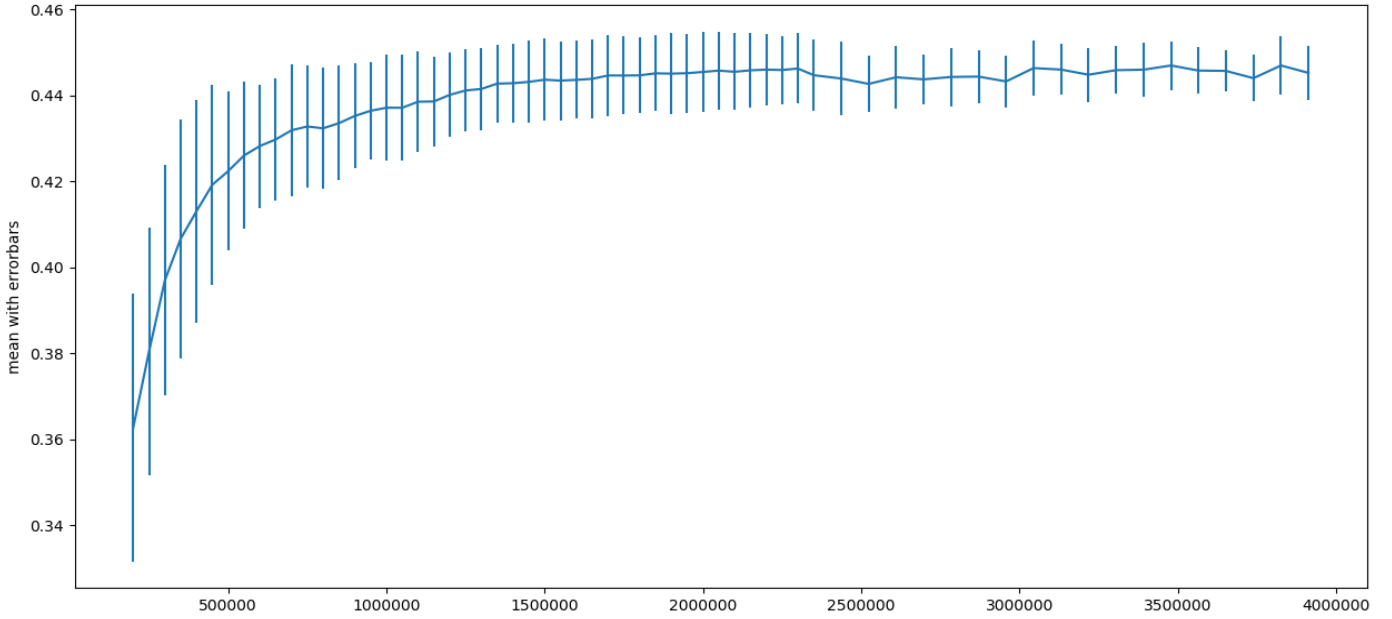
Fig. 4.1: Mean with errorbars of $simFC\text{-}empFC$ correlation depending on the simulation length in dt (ms/10), averaged for different parameter values

the individuals, this might be showing that abnormalities in $empFC$ of schizophrenia patients cannot be predicted as good as healthy controls. However, if the reason that GW data set can predict better compared to other data set is due to the higher imaging quality as discussed that the goodness of fit not only depends on the model selection but also the imaging quality of the SC matrix in [12], should be further studied and a better understanding of the effects of the underlying SC is needed in order to understand the actual reasons that enable such an observation.

For the $simFCD\text{-}empFCD$, where we evaluate the changes in functional connectivity over time, we have seen a data set specific fits, where $GW\text{-}GW$ predictions were better compared to the $HC/SCZ\text{-}HC/SCZ$ predictions, but they were much better compared to the $GW\text{-}HC/SCZ$ predictions, suggesting that we might see the effects of underlying SC and imaging parameters more obviously in the change of the functional connectivity over time.

For both the $simFC\text{-}empFC$ correlations and the $simFCD\text{-}empFCD$ KS-distance, we didn't see subject specific fits, i.e the SC matrix of individual i could predict neither $empFC$ nor $empFCD$ of the individual i better than the SC that belongs to the other individuals, rather we have seen differences across data sets. Lack of subject specificity is not special to the FHN model, rather can also be seen in the Stefanescu-Jirsa Hindmarsh-Rose 3D model [18]. The most straight forward explanation for the lack of subject specificity is the lack of differences in different SC matrices compared to the $empFC$ matrices, however if the reasons for this homogeneity in SC matrices is caused by an anatomical phenomenon or the

differences in imaging techniques should be further studied.

As we have discussed in the results section, we see a relatively high degree of agreement on the optimal working points of $simFC$-$empFC$ correlations in the I_{ext}/K space, where we can identify two regions that are likely to contain the optimal working points (2nd and 3rd regions), which interestingly coincide with the optimal working points of $simFC$-$simFC$, $simFC$-SC and with the interesting regions in Kuramoto order parameter space of both $simBOLD$ and FHN output. To the contrary of [15, 10, 22], we don't only see optimal working points at the edge of bifurcation points, where the underlying SC can influence greatly the noisy excursions, we see a set of optimal fits that are close to the bifurcation point for low global coupling, yet decreases as the global coupling increases. One of the intuitive explanation might be that, as both I_{ext} and the external input (i.e K and SC) have the same structure in the FHN equation (i.e additive), the external input might be compensating for the decreasing I_{ext}. This hypothesis might as well explain why we see $simFC$-$simFC$ and $simFC$-SC correlations at similar parameter combinations, however for a conclusive argument, further understanding of the underlying dynamics is necessary.

Furthermore, depending on the data-set of the SC matrix, the degree of agreement in the optimal working points w.r.t I/K varies, where the HC-SCZ (except the individual 35 that is an outlier) data set are much more homogeneous and the optimum working points are found mostly on the 2nd and 3rd regions, compared to the GW data set, where both inter- and intra data set variations are higher, because there are optimal points in the elliptical region as well as the two other regions.

Due to the incommensurability of the different parameters, as we have explained in the methodology, we have analyzed the I_{ext}/K and the c/σ space separately. We observed that, the parameter c has the least significant effect on the FHN network as discussed in [18], where we can also confirm this visually at the plotted spaces for all of the metrics used in this study (see: A.2), however the effects of the parameter σ on the $simFC$-$empFC$ correlation depends on the used data set and underlying SC regardless of the $empFC$'s , where for the GW data set we see the optimal working points for high σ values and for the other data sets lower σ values are preferred. However, much of the variance in the correlation values can be described by the I and K parameters, thus the extent of the importance of the noise for the FHN model, definitely being not zero, should may not be as much as in the other models as discussed in [11].

Finally, we can visually confirm from the averaged $simFC$-$empFC$ parameter space plots and also from the KS-test of the distance matrix of I/K parameter space distributions, that the underlying SC shapes the optimal working values stronger than the compared $empFC$.

In the result section, we have ignored the optimal working points of the $simFCD$-$empFCD$ KS distance, and the reason is that we were not able to find an agreement on the optimal parameters for I_{ext}/K space, but rather the optimal working points can be found in any I_{ext} value. It should also be noted that the 2nd region (as it might be related to the bifurcation point) shows generally good $simFCD$-$empFCD$ fits, though it is usually not the optimal working point. However when we evaluate the worst working points of the $simFCD$-

$empFCD$ KS distance, we observe an interestingly precise agreement around the lower bifurcation point and lower σ values regardless of the K and c values, which again contradicts with the previous findings of [15, 10, 22, 18]. However, we lack an intrinsic understanding of the underlying dynamics that could possibly allow us to relate the bifurcation points, optimal working points of $simFC$-$empFC$ and worst points of $simFCD$-$empFCD$. Furthermore, if the lack of good inter data-set prediction is caused by the lack of comprehensiveness of the FHN model, by variations in the underlying SC or by another reason cannot be answered at this point.

When we have evaluated $simFC$-SC, we have observed subject specificity and a significant effect of the underlying SC matrix on the $simFC$ similar to the [18]. However this doesn't necessarily indicate that SC is an important predictor of $simFC$ for all of the parameter combinations. When we don't consider only the best 15 parameter combination, we observe that all of the high $simFC$-SC correlation points are found in high σ values and gathered in two regions: the edges of the elliptical region in the middle (2nd region as identified before) and regions with low I_{ext} and high K values. Yet, to some extent, these results can be understood as parallel to the [21], where Messe argues that for even random networks, the (original) FHN model has a high agreement between SC-$simFC$.

Since we know that we can find a high $simFC$-SC correlation for some parameter combinations, and a high SC-SC correlation, we also evaluate the $simFC$-$simFC$ correlation values, in order to be able to distinguish the effects of the model and effects of the underlying SC on the $simFC$. We have already mentioned that for intra-GW data-set, we have found a higher correlation of SC-SC predictions and $simFC$-$simFC$ predictions compared to other data-sets, and also we have observed that the optimal working points with respect to $simFC$-$simFC$ correlation depend on the data set used, i.e for GW we have found optimal working points at the edges of the elliptical region (as in the $simFC$-SC case), and for $HC\&SCZ$ data sets the best correlation values are found on the 3rd line as identified previously.

When we further evaluate the complete parameter space of $simFC$-$simFC$ correlations, we see that for all of the data sets there are 2 trends, where the high correlation values are found: edges of the elliptical region with high σ values as in the $simFC$-SC correlations, and on the 3rd line as identified previously with low σ values, where $simFC$-SC performs poorly. Even though we can possibly explain the first trend with the effects of SC on the $simFC$ if we ignore the contribution of high σ values, we cannot use a similar explanation for the second trend. We therefore believe that this phenomenon rather than being related to the underlying SC matrix, is related to other effects such as the dynamics of FHN networks might play an important role, since the high correlation points of $simFC$-$simFC$ coincide with best $simFC$-$empFC$ fit points, and also the I_{ext} values are very close to lower bifurcation point for low K values, and I_{ext} values decrease as the K value increases. However, it is not clear at this point, if these results can be interpreted parallel to the hypothesis that parameters that are close to the Hopf bifurcation cause unique dynamics as in [10, 15, 22].

EXPLAIN HERE NOISE EFFECT ON BW MODEL + VECTOR SCALING

Lastly, we have put our prior belief that the choice of parameter $maxbold$ has a relatively insignificant effect to a test, and conducted a grid search on 4 different individuals with varying $maxbold$ values. We have observed, that especially for high σ values, $simFC$-$simFC$ correlations of differently scaled FHN outputs are very high. We believe that one of the possible explanation for this phenomenon might lie in the Eq.2.8, where both of the parameter s (activity dependent signal) and the parameter f_{in} (blood inflow) have a very low standard deviation (<0.5 for the observed cases) compared to the parameter z (the FHN output), which takes a value between 0 and $maxbold$, therefore acting as a constant with some degree of noise.

References

[1] Lynall M, Bassett D, Kerwin R, McKenna P, Kitzbichler M, Muller U, et al. Functional Connectivity and Brain Networks in Schizophrenia. Journal of Neuroscience. 2010;30(28):9477–9487. Available from: `doi.org/10.1523/jneurosci.0333-10.2010`.

[2] Friston K, Frith C. Schizophrenia: A Disconnection Syndrome. Clinical Neuroscience. 1995;3:89–97.

[3] Friston K. The disconnection hypothesis. Schizophrenia Research. 1998;30(2):115–125. Available from: `doi.org/10.1016/s0920-9964(97)00140-0`.

[4] Bullmore E, Frangou S, Murray R. The dysplastic net hypothesis: an integration of developmental and dysconnectivity theories of schizophrenia. Schizophrenia Research. 1997;28(2-3):143–156. Available from: `doi.org/10.1016/s0920-9964(97)00114-x`.

[5] Honey C, Kotter R, Breakspear M, Sporns O. Network structure of cerebral cortex shapes functional connectivity on multiple time scales. Proceedings of the National Academy of Sciences. 2007;102(24):10240–10245. Available from: `doi.org/10.1073/pnas.0701519104`.

[6] Dong D, Wang Y, Chang X, Luo C, Yao D. Dysfunction of Large-Scale Brain Networks in Schizophrenia: A Meta-analysis of Resting-State Functional Connectivity. Schizophrenia Bulletin. 2017;44(1):168–181. Available from: `doi.org/10.1093/schbul/sbx034`.

[7] Weber S, Johnsen E, Kroken R, Loberg E, Kandilarova S, Stoyanov D, et al. Dynamic Functional Connectivity Patterns in Schizophrenia and the Relationship With Hallucinations. Frontiers in Psychiatry. 2020;11.

[8] Hu M, Zong X, Mann J, Zheng J, Liao Y, Li Z, et al. A Review of the Functional and Anatomical Default Mode Network in Schizophrenia. Neuroscience Bulletin. 2016;33(1):73–84. Available from: `doi.org/10.1007/s12264-016-0090-1`.

[9] Ruan H, Luo Q, Palaniyappan L, Lu W, Huang C, Zac C, et al. Topographic diversity of structural connectivity in schizophrenia. Schizophrenia Research. 2020. Available from: `doi.org/10.1016/j.schres.2019.10.034`.

[10] Deco G, Ponce-Alvarez A, Mantini D, Romani G, Hagmann P, Corbetta M. Resting-State Functional Connectivity Emerges from Structurally and Dynamically Shaped Slow Linear Fluctuations. Journal of Neuroscience. 2013;33(27):11239–11252. Available from: `doi.org/10.1523/JNEUROSCI.1091-13.2013`.

[11] Deco G, Jirsa V, McIntosh A, Sporns O, , Kotter R. Key role of coupling, delay, and noise in resting brain fluctuations. Proceedings of the National Academy of Sciences. 2009;106(25):10302–10307. Available from: `doi.org/10.1073/pnas.0901831106`.

[12] Cabral J, Hugues E, Sporns O, Deco G. Role of local network oscillations in resting-state functional connectivity. NeuroImage. 2011;57(1):130–139. Available from: `doi.org/`

`10.1016/j.neuroimage.2011.04.010.`

[13] Ghosh A, Rho Y, McIntosh A, Kotter R, Jirsa V. Cortical network dynamics with time delays reveals functional connectivity in the resting brain. Cognitive Neurodynamics. 2008;2(2):115–120. Available from: `doi.org/10.1007/s11571-008-9044-2.`

[14] Honey C, Sporns O, Cammoun L, Gigandet X, Thiran J, Meuli R, et al. Predicting human resting-state functional connectivity from structural connectivity. Proceedings of the National Academy of Sciences. 2009;106(6):2035–2040. Available from: `doi.org/10.1073/pnas.0811168106.`

[15] Ghosh A, Rho Y, McIntosh A, Kotter R, Jirsa V. Noise during Rest Enables the Exploration of the Brains Dynamic Repertoire. PLoS Computational Biology. 2008;4(10). Available from: `doi.org/10.1371/journal.pcbi.1000196.`

[16] Ipina I, Kehoe P, Kringelbach M, Laufs H, Ibanez A, Deco G, et al. Modeling the relationship between regional activation and functional connectivity during wakefulness and sleep. 2019.

[17] Rolls E, Joliot M, Tzourio-Mazoyer N. Implementation of a new parcellation of the orbitofrontal cortex in the automated anatomical labeling atlas. NeuroImage. 2015;122:1–5. Available from: `doi.org/10.1016/j.neuroimage.2015.07.075.`

[18] Zimmermann T, Zimmermann J, Stefanovski L, Roy D, Solodkin A, Jirsa V, et al. Identifying optimal working points of individual Virtual Brains: A large-scale brain network modelling study. bioRxiv. 2020. Available from: `doi.org/10.1101/2020.03.26.009795.`

[19] Vuksanovic V, Hovel P. Large-Scale Neural Network Model for Functional Networks of the Human Cortex. Selforganization in Complex Systems: The Past, Present, and Future of Synergetics. 2015:345–352. Available from: `doi.org/10.1007/978-3-319-27635-9_26.`

[20] Messe A, Rudrauf D, Benali H, Marrelec G. Relating Structure and Function in the Human Brain: Relative Contributions of Anatomy, Stationary Dynamics, and Non-stationarities. PLoS Computational Biology. 2014;10(3). Available from: `doi.org/10.1371/journal.pcbi.1003530.`

[21] Messe A, Hutt M, Konig P, CC H. A closer look at the apparent correlation of structural and functional connectivity in excitable neural networks. Scientific Reports. 2015;5(1). Available from: `doi.org/10.1038/srep07870.`

[22] Deco G, Kringelbach M, Jirsa V, Ritter P. The dynamics of resting fluctuations in the brain: metastability and its dynamical cortical core. Scientific Reports. 2017;7(1). Available from: `doi.org/10.1038/s41598-017-03073-5.`

[23] Behrens T, Johansen Berg H, Jbabdi S, Rushworth M, MW W. Probabilistic diffusion tractography with multiple fibre orientations: What can we gain? NeuroImage. 2007;34(1):144–155.

[24] Woolrich M, Ripley B, Brady M, Smith S. Temporal Autocorrelation in Univariate Linear Modeling of FMRI Data. NeuroImage. 2001;14:1370–1386. Available from: `doi.org/10.1006/nimg.2001.0931`.

[25] Salimi-Khorshidi G, Douaud G, Beckmann C, Glasser M, Griffanti L, Smith S. Automatic denoising of functional MRI data: Combining independent component analysis and hierarchical fusion of classifier. NeuroImage. 2014;90:449–468. Available from: `doi.org/10.1016/j.neuroimage.2013.11.046`.

[26] Griffanti L, Salimi-Khorshidi G, Beckmann C, Auerbach E, Douaud G, Sexton C, et al. ICA-based artefact removal and accelerated fMRI acquisition for improved resting state network imaging. NeuroImage. 2014;95:232–247. Available from: `doi.org/10.1016/j.neuroimage.2014.03.034`.

[27] Friston K, Harrison L, Penny W. Dynamic causal modelling. NeuroImage. 2003;19(4):1273–1302. Available from: `doi.org/10.1016/S1053-8119(03)00202-7`.

[28] Knocka S, McIntosh A, Sporns O, Kotter R, Hagmannh P, Jirsaa V. The effects of physiologically plausible connectivity structure on local and global dynamics in large scale brain models. Journal of Neuroscience Methods. 2009;183(1):86–94. Available from: `doi.org/10.1016/j.jneumeth.2009.07.007`.

[29] Fitzhugh R. Impulses and Physiological States in Theoretical Models of Nerve Membrane. Biophysical Journal. 1961;1(6):445–466. Available from: `doi.org/10.1016/S0006-3495(61)86902-6`.

[30] Kostova T, Ravindran R, Schonbek M. Fitzhugh-nagumo Revisited: Types of bifurcations, Periodical Forcing and Stability Regions by a Lyapunov Functional. International Journal of Bifurcation and Chaos. 2003. Available from: `doi.org/10.1142/S0218127404009685`.

[31] Cakan C, Obermayer K. Biophysically grounded mean-field models of neural populations under electrical stimulation. 2020;16(4). Available from: `doi.org/10.1371/journal.pcbi.1007822`.

[32] Frackowiak R, Ashburner J, Penny W, Zeki S. Human Brain Function 2nd edition. Friston KJ, Frith CD, Dolan RJ, Price CJ, Mittelbach F, Samarin A, editors. Academic Press; 2004.

[33] Beckmann C, DeLuca M, Devlin J, Smith S. Investigations into resting-state connectivity using independent component analysis. Philosophical Transactions of the Royal Society B: Biological Sciences. 2005;360(1457):1001–1013. Available from: `doi.org/10.1098/rstb.2005.1634`.

[34] Damarajua E, Allena E, Belgerc A, Fordd J, McEwenf S, Mathalond D, et al. Dynamic functional connectivity analysis reveals transient states of dysconnectivity in schizophrenia. NeuroImage: Clinical. 2014;5:298–308. Available from: `doi.org/10.1016/j.nicl.2014.07.003`.

[35] Kuramoto Y. Chemical oscillations, waves, and turbulence. Courier Corporation; 2003.

[36] Scott D. Multivariate Density Estimation: Theory, Practice, and Visualization. New York, Chicester: John Wiley & Sons; 1992.

[37] Silverman B. Density Estimation for Statistics and Data Analysis. London: Chapman and Hall; 1986.

[38] Wand M, Jones M. Kernel Smoothing (Monographs on Statistics and Applied Probability). Springer; 1995.

[39] Kailath T. The Divergence and Bhattacharyya Distance Measures in Signal Selection. IEEE Transactions on Communications. 1967;15:52–60. Available from: `doi.org/10.1109/tcom.1967.1089532`.

A. Section 4

A.1. Emprical Data Analysis

A.2. Simulated Data Analysis

A.3. $maxbold$ Parameter